Received 21 October 2023; revised 27 November 2023; accepted 16 December 2023. Date of publication 19 December 2023; date of current version 8 January 2024.

Digital Object Identifier 10.1109/OJCOMS.2023.3344582

STAR-RIS Empowered NOMA Systems With Caching and SWIPT

THAI-HOC VU [1] (Graduate Student Member, IEEE), ANAND JEE [2] (Graduate Student Member, IEEE), DANIEL BENEVIDES DA COSTA [3] (Senior Member, IEEE), AND SUNGHWAN KIM [1] (Senior Member, IEEE)

[1]Department of Electrical, Electronic and Computer Engineering, University of Ulsan, Ulsan 44610, Republic of Korea
[2]Department of Electrical Engineering, Indian Institute of Technology Delhi, New Delhi 110016, India
[3]Digital Science Research Center, Technology Innovation Institute, Abu Dhabi, UAE

CORRESPONDING AUTHOR: S. KIM (e-mail: sungkim@ulsan.ac.kr)

This work was supported by the 2023 Research Fund of University of Ulsan.

ABSTRACT This paper proposes the joint use of caching and simultaneous wireless information and power transfer (SWIPT) to enhance the performance of cell-edge users of down-uplink simultaneously transmitting and reflecting reconfigurable intelligent surface (STAR-RIS)-empowered non-orthogonal multiple access (NOMA) systems. The main idea is to leverage the available caching at nearby users to establish cooperative communication while taking into account the problem of energy issues through SWIPT mechanisms, namely time-switching (TS) and power-splitting (PS) strategies. To improve the communication quality of users, STAR-RIS with an energy-splitting (ES) protocol is established and phase-shift design is formulated. Closed-form approximations and asymptotic expressions for users' outage probability (OP) and effective ergodic capacity (EC) are derived. Based on the attained expressions, useful insights into system design, such as the impact of power allocation, imperfect successive interference cancellation, the number of transmit/reflect components on the system performance, trade-offs between the network requirement and the system performance, and trade-offs between the energy harvesting process and data transmission quality, are deduced. Numerical examples verify our derivations and show that: **i**) the performance of cell-edge users is improved significantly; **ii**) exploiting SWIPT-PS shows better OP and EC performance for nearby users compared to SWIPT-TS, while both provide comparable performance for cooperative communication; **iii**) as the performance of cell-edge users is mostly guaranteed, the communication quality of nearby users in downlink and source node in uplink can be improved by optimizing either the power budget or the energy harvesting factors; **iv**) adopting STAR-RIS with ES protocol outperforms mode-switching and time-splitting ones in terms of both OP and EC; and **v**) STAR-RIS-empowered NOMA has better EC performance than orthogonal-multiple access counterparts when SIC operation is properly designed.

INDEX TERMS Cache-aided communications, imperfect successive interference cancellation (SIC), non-orthogonal multiple access (NOMA), simultaneously transmitting and reflecting reconfigurable intelligent surface (STAR-RIS), simultaneous wireless information and power transfer (SWIPT).

I. INTRODUCTION

RECENTLY, wireless local area networks have become essential in Internet-of-things (IoT) based smart homes, businesses, and day-to-day public facilities [1]. Wireless technologies have widely adapted for modern IoT devices like smartphones, smart wearables, smart homes, and smart cities. With around forty billion devices expected to connect to the Internet by 2025, the demand for massive connectivity in beyond fifth-generation (5G) networks is significantly increasing to support wireless data services with enhanced

connectivity [2] and nearby zero-latency [3], for example, ultra-high video resolution, metaverse, and video conferencing [4]. These features introduce challenges for architectural innovation in wireless transmissions involving new multiple access paradigms, sustainable communications, and efficient uses of resources [5].

Multiple access techniques have played a vital role in improving the capacity of communication networks. Over the decade, the evolution of orthogonal multiple access (OMA) paradigms, which mostly focused on exploiting frequency/time/code division, is to mitigate interference but is no longer capable of accommodating an increasing number of users due to limited resources [6]. Driven by this fact, non-orthogonal multiple access (NOMA) has emerged as a potential candidate by means of multiplexing user signals in the power domain to obtain the same frequency/time/code resource blocks [7]. Thanks to leveraging successive interference cancellation (SIC) techniques [8], NOMA has effectively dealt with limited connectivity and inefficient spectrum uses, while also demonstrating flexibility and efficient energy utilization [9]. Besides, it was demonstrated to have a higher throughput compared to OMA techniques [10]. As a result, NOMA has gained attention in communication standards due to recent advancements and promising experimental outcomes. For example, in Release 13 long-term evolution (LTE) of the Third Generation Partnership Project (3GPP), NOMA was proposed as multi-user superposition transmission for downlink mobile broadband services [11]. Additionally, 3GPP's release-14 and release-15 were designed for uplink transmissions to support a large number of devices and enable ultra-reliable low-latency communication (URLLC) through grant-free transmission [12].

Recently, reconfigurable intelligent surface (RIS) has gained popularity as a sustainable communication solution that aims to achieve low-cost implementation, enhanced spectrum utilization, robust energy efficiency, and connection formation in difficult-to-reach areas [13]. An RIS typically consists of multiple tunable reflective passive elements that are capable of changing the phase of incoming electromagnetic signals, allowing it to control wireless signal movement [14] as well as to increase signal strength at the receiver node while compensating for performance loss caused by wireless propagation [15]. Due to its basic functionality of intelligently reconfiguring the radio propagation environment, RIS can further achieve robust spectrum utilization by providing simultaneous bidirectional transmissions [16]. Therefore, research in RIS areas has received significant interest, such as downlink and uplink wireless-based RIS transmissions [17], [18], [19], optimizing phase-shift configuration for spectral efficiency enhancement [20], [21], [22], leveraging RIS for reliability and security transmissions [23], [24], [25], [26], and improving system energy efficiency through simultaneously wireless information and power transfer (SWIPT) mechanisms [27], [28], [29] and wireless powered solutions [30].

With advancements in reflective and transmissive metasurfaces, an upgraded version of RIS called simultaneously transmitting and reflecting RIS (STAR-RIS) has recently appeared as an innovative approach that provides full 360-degree coverage [31]. The feasibility of STAR-RIS is showcased with mixed indoor and outdoor scenarios, and what is unique about STAR-RIS is the way it splits the incoming signal into two parts: 1) the transmitted signal, which aims at the region behind the RIS; and 2) the reflected signal, which is directed towards the area in front of the RIS. These are basically referred to as the refraction region and the reflection region. Compared to traditional RIS, this approach entails a significant enhancement in terms of practicality and reliability [32]. Hence, research on STAR-RIS has received considerable attention from the scientific community under different perspectives, combination with energy-splitting, mode-switching (another version called partitions), and time-splitting protocols [33], [34], improving spectrum utilization with NOMA [35], enhancing URLLC networks [36], secured communication [37], and towards sustainable and efficient communications with SWIPT interaction [38], [39].

On another front, developing resource-efficient solutions plays a pivotal direction in future communication networks. By exploiting the availability of resource data within networks, wireless caching technology helps bringing data closer to users [40]. This strategy alleviates the burden on base stations and network backhaul limitations. Based on its implementations, caching methods fall into two categories: one relies on dedicated storage infrastructure like content servers, aiming to pre-position data efficiently before user requests [41]; and the other, known as caching-based individual nodes [42], enables users to collaboratively share available cached content using device-to-device (D2D) communications and only communicate with base stations when local options fail. Compared to the former [41], exploiting the latter approach [42] yields more flexible and efficient communications as it does not require any overhead for network deployment. As a consequence, research on caching-based individual nodes has been showing its feasibility in a variety of contexts to enhance the system's spectrum utilization [43], [44], [45], [46] and cell-edge users' performance [47], [48], [49], [50]

From the aforementioned discussions, it is clear that caching is a key part of future communication networks and remains relatively unexplored in conjunction with emerging technologies, such as NOMA, STAR-RIS, and SWIPT. In particular, as shown in [44], [45], exploiting caching at nearby users in coordinated NOMA systems can efficiently mitigate the impact of inter-relaying interference. Meanwhile, the works in [48] confirmed that a cache-equipped helper with SWIPT capability can reach the goal of maximizing the sum rate while meeting minimum quality-of-service (QoS) requirements. On the other hand, it was also demonstrated in [49], [50] that the use of the caching solution in wireless communication networks with SWIPT-enabled

TABLE 1. Summary of literature: techniques and contributions.

Papers	RIS	STAR-RIS	NOMA	SWIPT	Caching	Contributions
[15]-[26]	✓					RIS versus conventional relay [16]; Beamforming design [15], [21], [25]; rate maximization [19]; closed-form OP for Rician [17] and Nakagami-m channels [18]; error-phase RIS modeling [20], [21]; spectrum and energy efficiency trade-off [22]; OP analysis of full-duplex with one way [24] and two-way communications [23]; RIS-aided secure communication [25], [26].
[28]-[30]	✓			TS or PS		Alternating algorithms for high-quality suboptimal solutions and reduced computational complexity [28]; robust beamforming design with cascaded channel imperfections [29]; there dynamic beamforming designs [30].
[32]-[37]		✓	↘ or ↖			Dual-sided function [32], Practical protocols [33]; near and far-field modelings [34]; analysis of modulation [35]; short-blocklength [36]; enhanced security [37].
[38], [39]		✓	↘	✓		Resource allocation [38]; enhancing mobile edge computing [39].
[43]-[45]			↘		✓	Inter-user interference mitigation scheme-based caching solution [44], [45]; dynamic detection-based caching interference cancellation [43].
[46],[47]					✓	A D2D aided multi-antenna coded caching scheme to exploit local data exchange among nearby users [46]; a new distributed caching design-based link scheduling and power control property [47].
[48]-[50]			↘ or ↖	TS or PS	✓	A two-stage content push and transmission scheme [48]; an algorithm for improving latency and energy efficiency of helper nodes [49]; coordinated cognitive paradigms with wireless caching and SWIPT [50].
This paper		✓	↘ + ↖	TS + PS	✓	An efficient caching and SWIPT scheme for low-cost deployment; consider the use of both SWIPT-PS and SWIPT-TS; analysis of imperfect SIC and STAR-RIS with error-phase alignment; closed-form approximate and asymptotic expressions for OP and EC; comparative performance of STAR-RIS operating protocols; investigating impacts of PA policy and the design of SWIPT and STAR-RIS.

Note: ✓ (yes), ↘ (downlink), ↖ (uplink), power allocation (PA), outage probability (OP), and ergodic capacity (EC).

NOMA signaling can not only improve spectrum utilization but also achieve sustainable and energy-efficient communications. However, there is a fact that the adoption of SWIPT might be not effective for devices equipped with caching solutions when the source node has a small number of antennas, especially the single-antenna cases. This is because limited devices demand the use of higher signal fractions for their information signal processing when dealing with the SWIPT-based power-splitting (PS) relaying strategy, causing energy reduction for cooperative communications [51]. Similarly, for the SWIPT-based time-switching (TS) mechanism, harvesting energy in a short time might also not have enough power for caching-aided transmissions. Fortunately, the presence of RIS, and in particular STAR-RIS, offers an alternative solution. As pointed out in [27], the lifespan of low-power IoT networks can be extended with SWIPT-integrated RIS solutions. Similarly, the work in [28] revealed that throughout the joint design of precoding matrices, RIS matrix, and the PS ratio, SWIPT-enabled RIS can overcome problems of nonlinear energy harvesting implementations. Also, the realization of a SWIPT-based RIS solution can improve the system performance when dealing with imperfect channel estimation procedures [29]. Furthermore, the recent studies also verified that the integration of STAR-RIS and SWIPT mechanisms can maximize the sum rate with TS protocol [38] while also improving the efficiency of energy transfer and task offloading in wireless-powered mobile edge computing [38], [39].

However, the potential and efficient interplay of caching and SWIPT solutions with STAR-RIS-based NOMA systems has not been covered in the literature yet, to the best of the authors' knowledge. Motivated by this fact, this paper considers the integration of NOMA, STAR-RIS, and SWIPT.

A. CONTRIBUTIONS AND OUTCOMES

The research conducted in this work delves into exploring the potential of utilizing STAR-RIS-empowered NOMA systems in conjunction with caching and SWIPT solutions. The primary objective is to leverage the availability of nearby users' caching to enhance the performance quality of cell-edge users. To address the power budget constraints, two energy harvesting mechanisms, namely SWIPT-TS and SWIPT-PS, are analyzed for nearby users. Additionally, to augment the user's communication quality in downlink/uplink and ensure low-complexity implementations, STAR-RIS designs are quantified using an energy-splitting (ES) protocol and a suboptimal phase-shift alignment. To facilitate practical implementations, a non-ideal SIC receiver is examined for both nearby users and source nodes. The key contributions of this paper can be summarized as follows:

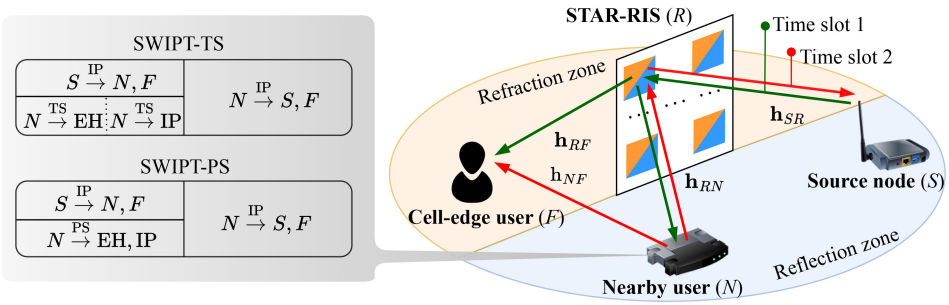

FIGURE 1. Illustration of the proposed transmission model.

- This work, for the first time, studies the performance of STAR-RIS-empowered NOMA systems by relying on caching and SWIPT at nearby users to enhance cell-edge users' performance while increasing the system's spectral utilization efficiently.
- Towards providing a comprehensive performance while being aware of practical implementations, two quantitative SWIPT mechanisms, namely SWIPT-TS and SWIPT-PS, are presented. Also, the implementation of imperfect SIC and the alignment of discrete phase-shift configurations at STAR-RIS have also been evaluated.
- Analysis of the proposed system with SWIPT-TS and SWIPT-PS has been conducted in terms of OP and effective EC, in which closed-form approximate expressions are derived followed by an asymptotic analysis at high signal-to-noise ratio (SNR) regime. Accordingly, several discussions have been revealed to offer valuable engineering insights into system designs.
- A performance study of STAR-RIS-empowered NOMA and OMA has been conducted. Numerical results confirm that: 1) With the proposed solution, the performance of CE is improved significantly; 2) Compared to SWIPT-TS, nearby users achieve more efficient OP and EC performance when adopting SWIPT-TS mechanisms. However, both techniques offer comparable performance for cooperative communications; 3) As cell-edges' performance is usually guaranteed, optimizing either the power budget or energy harvesting factors can further improve the communication quality of nearby users in downlink transmissions and source node in cooperative communications; 4) The adoption of STAR-RIS with ES protocol provides better OP and EC performance than those of mode-switching and time-splitting ones; and 5) When SIC operations are properly designed, STAR-RIS-empowered NOMA outperforms OMA counterparts at most SNR regimes.

B. MATHEMATICS AND NOTATIONS

$F_X(\cdot)$ and $f_X(\cdot)$ are the cumulative distribution function (CDF) and probability density function (PDF) of a random variable X, respectively. $\Gamma(\cdot,\cdot)$ and $\Gamma(\cdot)$ are the corresponding upper incomplete Gamma and Gamma functions. $G_{\cdot,\cdot}^{\cdot,\cdot}(\cdot|_{\cdot,\cdot}^{\cdot,\cdot})$ and $G_{\cdot,\cdot,\cdot,\cdot,\cdot,\cdot}^{\cdot,\cdot,\cdot,\cdot,\cdot,\cdot}(\cdots|\cdots|\cdots|\cdot,\cdot)$ denote the Meijer-G function [52, eq. (9.301)] and the extended generalized bivariate Meijer-G function [53, eq. (3)], respectively. $\mathcal{K}_0(\cdot)$ is the zero-order modified Bessel function of the second kind [52, eq. (8.407.2)].

II. SYSTEM MODEL

A. SYSTEM DESCRIPTION

Let us consider a typical STAR-RIS empowered SWIPT NOMA system, as shown in the right-hand side of Fig. 1, which includes a single-antenna source (S), a nearby user (N), a cell-edge user (F), and a STAR-RIS (R) with K elements. In the considered system,[1] there is no connection between S and users due to blockages. N and F are placed in refraction and reflection zones of STAR-RIS, respectively. The STAR-RIS is established to assist the communication from S to users as well as the cooperative communication from N to S and F thanks to ES protocols [33], [34].

The communication is composed of two main stages, with each stage having the same duration T. In the first stage, with the assistance of R, the source node serves users simultaneously using NOMA. Then, while F with weaker channel conditions retains the received signal for the second stage, N with better channel conditions utilizes SIC to decode the decoded message of F, then saves this message in its cache[2] for the next process instead of removing them as in traditional thought [7], and finally decodes its own message. In the second stage, N will exploit NOMA to superimpose its feedback together with the prior decoded message of F and then forward this superposition encoding to S and F thanks to the aid of R. Following that, S uses SIC to separate its received signal while F relies on a selection combining technique to combine the previously received signal and the newly incoming signal to increase its decoding probability.

However, N might have not enough energy to conduct the cooperative communication due to a limited power budget. Thus, it is assumed that N is equipped with SWIPT-TS or SWIPT-PS receivers [28], [50] that enable it to harvest energy from the reflective signal generated by STAR-RIS

1. When dealing with dynamic and dense networks that involve multiple users and often encounter interference, the considered system can be regarded as a fundamental block of hybrid OMA-NOMA schemes [54].

2. Exploiting caching gives more chances to improve cell-edge users' performance, especially when RIS and cell-edge links are blocked.

in the first communication stage, as shown in the left-hand side of Fig. 1. Nevertheless, to give rise chance for N to have sufficient harvested energy while also improving the performance quality of users, STAR-RIS is established with a large number of RIS elements, and the phase-shift alignment must be configured so that the received channel at users is maximized. Similar to [36], we consider the sub-optimal phase-shift alignment to be tuned to the discrete phase-shift model with low computational complexity. At STAR-RIS, the diagonal phase shift matrix Φ^s, which simultaneously assists the intended messages of N (x_n) in reflection zones and F (x_f) in refraction zones, can be characterized by

$$\Phi^s = \text{diag}\big(\sqrt{\eta_1^s}e^{j\phi_1^s}, \sqrt{\eta_2^s}e^{j\phi_2^s}, \ldots, \sqrt{\eta_K^s}e^{j\phi_K^s}\big),$$

where $\eta_k^s \in (0, 1]$ is the ES factor for signal $x_s \in \{n, f\}$ and $\phi_k^s \in (-\pi, \pi]$ is the phase shift of the k-th RIS element, with $k = 1, 2, \ldots, K$, and the ES factor must hold $\eta_k^n + \eta_k^f = 1$. The strategy for aligning ϕ_k^s can be described as follows: 1) Reflective zones: $\phi_k^n = -\arg(g_{SR}) - \arg(g_{RN}) + \phi_e$; and 2) Refractive zones: $\phi_k^f = g_{NF} - \arg(g_{RF}) - \arg(g_{NR}) + \phi_e$. Herein, ϕ_e represents the quantized phase-error, obeying Uniform distribution $\mathcal{U}(-2^{-q}\pi, 2^{-q}\pi)$, with q being a finite number of control bits.

Denote by h_{TxRx} the fading coefficient of transmitter (Tx)-receiver (Rx) links, where Tx, Rx $\in \{S, R, N, F\}$. h_{TxRx} obeys composite channel models and is mathematically represented by $h_{\text{TxRx}} = \sqrt{\Omega_{\text{TxRx}}}g_{\text{TxRx}}$, where Ω_{TxRx} stands for large-scale fading while g_{TxRx} presents the small-scale Rayleigh fading[3] with a unit scale parameter [17], [32], [35], [36]. The channel gain $|g_{\text{TxRx}}|^2$ is an exponential random variable with PDF of $f_{|g_{\text{TxRx}}|^2}(z) = \exp(-z), \forall z \geq 0$. Throughout this work, suppose that all channel state information (CSI) involving Tx-Rx links is statistically acquired and available at the terminals via the handshaking signal procedure [17], [18], [20], [21], [32], [33], [34], [35], [36], [37], which is typically done before the communication occurs, and the study of obtaining CSI is, thus, beyond the scope of this work.

The proposed transmission model can be realized in numerous practical scenarios of indoor, outdoor, mixed cellular and wireless IoT networks with the popularity of blocked objects (i.e., warehouses, factories, homes, offices, or shopping centres), where relay unit, access points, IoT devices, and/or sink nodes directly harvest energy from the reflective signals of STAR-RIS mounted on building, floor, window to forward the sounding physical phenomenon data from cellular base station,a centre access point, IoT node, and/or sink node to the target destination while feedback its response to source information nodes using NOMA.

3. Rayleigh fading channel is a prevalent model that captures the effect of numerous scatterers in propagation environments, such as buildings, trees, or atmospheric particles. Analyzing the performance under Rayleigh models can assess the resilience of a wireless system to multipath fading, which frequently occurs in urban areas as well as indoor and outdoor environments [24]. Furthermore, Rayleigh does not include any dominant line-of-sight component; thus, it serves as a useful benchmark to compare with other channel models, such as Rician or Nakagami-m [55].

B. SIGNAL MODEL, EFFECTIVE RATE, AND OUTAGE EVENTS

1) SWIPT-TS CRITERION

In the first stage, S employs NOMA to encode x_n and x_f as $x = \sqrt{aP_S}x_f + \sqrt{(1-a)P_S}x_n$, where a is the power allocation (PA) factor and P_S is the transmit power of S, with $\text{E}\{|x_n|^2\} = \text{E}\{|x_f|^2\} = 1$. In order to ensure the weaker user has detection of its own signal, the power budget assigned to F is higher than that of N, which means $a \in (0.5, 1)$. Then, S sends the symbol x to users. The received symbol at user W can be expressed as

$$y_W = \mathbf{h}_{SR}^T \Phi^s \mathbf{h}_{RW} x + n_W, \quad W \in \{N, F\} \tag{1}$$

where $n_W \sim \mathcal{CN}(0, \sigma^2)$ is the additive white Gaussian noise. During the transmission, N uses αT and $(1-\alpha)T$ time for energy harvesting and information process (IP), respectively. The energy harvested at N is computed as $E_N = \zeta\alpha T|\mathbf{h}_{SR}^T\Phi^n\mathbf{h}_{RN}|^2 P_S$, where $\zeta \in (0, 1)$ indicates the energy conversion efficiency. N uses SIC to separate x_f and x_n from y_N in (1) with the corresponding signal-to-interference-plus-noise ratios (SINRs) given by

$$\gamma_N^{x_f} = \frac{aP_S|\mathbf{h}_{SR}^T\Phi^n\mathbf{h}_{RN}|^2}{(1-a)P_S|\mathbf{h}_{SR}^T\Phi^n\mathbf{h}_{RN}|^2 + \sigma^2}, \tag{2}$$

$$\gamma_N^{x_n} = \frac{(1-a)P_S|\mathbf{h}_{SR}^T\Phi^n\mathbf{h}_{RN}|^2}{\Xi_N aP_S|\mathbf{h}_{SR}^T\Phi^n\mathbf{h}_{RN}|^2 + \sigma^2}, \tag{3}$$

where Ξ_N represents the remaining level of interference caused by SIC imperfections. Instead of normally discarding x_f, N stores x_f in its cache to improve F's performance through cooperative communication in the next phase. At F, the SINR to decode x_f from y_F can be written as

$$\gamma_F^{x_f} = \frac{aP_S|\mathbf{h}_{SR}^T\Phi^f\mathbf{h}_{RF}|^2}{(1-a)P_S|\mathbf{h}_{SR}^T\Phi^f\mathbf{h}_{RF}|^2 + \sigma^2}. \tag{4}$$

In the second stage, N adopts NOMA to multiplex $\bar{x}_f \triangleq x_f$ with its new feedback signal x_s into $\bar{x} = \sqrt{bP_N}\bar{x}_f + \sqrt{(1-b)P_N}x_s$, where $P_N = E_N/T = \zeta\alpha|\mathbf{h}_{SR}^T\Phi^n\mathbf{h}_{RN}|^2 P_S$ and $\text{E}\{|x_s|^2\} = \text{E}\{|\bar{x}_f|^2\} = 1$. Taking it for granted that the power budget assigned for $\bar{x}_f$ is set higher than that of x_s, i.e., $b \in (0.5, 1)$. The received symbol at S and F can be written, respectively, as

$$y_S = \mathbf{h}_{NR}^T\Phi^n\mathbf{h}_{RS}\bar{x} + n_S, \tag{5}$$

$$y_F = \Big(h_{NF} + \mathbf{h}_{NR}^T\Phi^f\mathbf{h}_{RF}\Big)\bar{x} + n_F, \tag{6}$$

where $n_M \sim \mathcal{CN}(0, \sigma^2)$. The respective SINRs at S to detect $\bar{x}_f$ and x_s transmitted from N can be written as

$$\gamma_S^{\bar{x}_f} = \frac{bP_N|\mathbf{h}_{NR}^T\Phi^n\mathbf{h}_{RS}|^2}{(1-b)P_N|\mathbf{h}_{NR}^T\Phi^n\mathbf{h}_{RS}|^2 + \sigma^2}, \tag{7}$$

$$\gamma_S^{x_s} = \frac{(1-b)P_N|\mathbf{h}_{NR}^T\Phi^n\mathbf{h}_{RS}|^2}{\Xi_S bP_N|\mathbf{h}_{NR}^T\Phi^n\mathbf{h}_{RS}|^2 + \sigma^2}, \tag{8}$$

where Ξ_S is the imperfect SIC indicator. Meanwhile, the received SINR at F to detect $\bar{x}_f$ can be given by

$$\gamma_F^{\bar{x}_f} = \frac{bP_N|h_{NF} + \mathbf{h}_{NR}^T \Phi^n \mathbf{h}_{RF}|^2}{(1-b)P_N|h_{NF} + \mathbf{h}_{NR}^T \Phi^n \mathbf{h}_{RF}|^2 + \sigma^2}. \quad (9)$$

Then, two signals from S and N are evaluated at F based on selection combining techniques with respective SINR as

$$\gamma_F^{\text{e2e}} = \max\{\gamma_F^{x_f}, \gamma_F^{\bar{x}_f}\}. \quad (10)$$

2) SWIPT-PS CRITERION

In the first stage, N harvests energy from y_N in (1) through the PS mechanism. In particular, the energy harvested by N is written as $E_N = \zeta\beta P|\mathbf{h}_{SR}^T \Phi^n \mathbf{h}_{RN}|^2 T$, where $\beta \in (0,1)$ denotes the PS ratio. Thus, the received signal for detecting information transmitted from S is given by $y_N = \sqrt{1-\beta}\mathbf{h}_{SR}^T \Phi^n \mathbf{h}_{RN} x + n_N$. Adopting SIC, the received SINRs at N to detect x_f and x_n are expressed as

$$\gamma_N^{x_f} = \frac{(1-\beta)aP_S|\mathbf{h}_{SR}^T \Phi^n \mathbf{h}_{RN}|^2}{(1-\beta)(1-a)P_S|\mathbf{h}_{SR}^T \Phi^n \mathbf{h}_{RN}|^2 + \sigma^2}, \quad (11)$$

$$\gamma_N^{x_n} = \frac{(1-\beta)(1-a)P_S|\mathbf{h}_{SR}^T \Phi^n \mathbf{h}_{RN}|^2}{\Xi_N(1-\beta)aP_S|\mathbf{h}_{SR}^T \Phi^n \mathbf{h}_{RN}|^2 + \sigma^2}. \quad (12)$$

Similar to SWIPT-TS for the second stage, N employs NOMA to forward $\bar{x}$ to S and F with $P_N = E_N/T = \zeta\beta|\mathbf{h}_{SR}^T \Phi^n \mathbf{h}_{RN}|^2 P_S$. The received SINRs at S and F to detect $\bar{x}_f$ and x_s are the same as those from (7) to (10).

3) EFFECTIVE RATES

Consider the decoding ability-based selective cooperative communication [8], from the formulated SINRs in (2), (3), (11), and (12), the effective rate of N conditioned on the target rate threshold r_f for decoding x_f is given by

$$\mathcal{R}_N = \left\{\frac{\omega}{2}\mathcal{R}\left(\gamma_N^{x_n}\right) : \frac{\omega}{2}\mathcal{R}\left(\gamma_N^{x_f}\right) \geq r_f\right\}, \quad (13)$$

where $1/2$ stands for the ratio between the consumed time T and the total network duration $2T$, $\mathcal{R}(\gamma) = \log_2(1+\gamma)$ is the Shannon capacity formula, and ω represents SWIPT operation mode. Herein, if SWIPT-TS is adopted, $\omega = 1-\alpha$. Inversely, when SWIPT-PS is considered, $\omega = 1$. Meanwhile, the effective rates of S and F conditioned on the successful decoding signals $\bar{x}_f$ and x_f are respectively determined as

$$\mathcal{R}_S = \left\{\frac{1}{2}\mathcal{R}\left(\gamma_S^{x_s}\right) : \frac{1}{2}\mathcal{R}\left(\gamma_S^{\bar{x}_f}\right) \geq r_f\right\}, \quad (14)$$

$$\mathcal{R}_F^{\text{e2e}} = \left\{\frac{1}{2}\mathcal{R}\left(\gamma_F^{x_f}\right) : \frac{\omega}{2}\mathcal{R}\left(\gamma_N^{x_f}\right) < r_f\right\} \bigcup \left\{\frac{1}{2}\mathcal{R}\left(\gamma_F^{\text{e2e}}\right) : \frac{\omega}{2}\mathcal{R}\left(\gamma_N^{x_f}\right) \geq r_f\right\}. \quad (15)$$

4) OUTAGE EVENTS

The outage event of a signal that is transmitted from the transmitter to the receiver is identified if the achievable information rate falls below a certain threshold rate [51].

Denote by r_n and r_s as the target rate thresholds for decoding x_n and x_s, respectively. The outage event at N can be defined as the unsuccessful decoding of either x_n or x_f. Using complementary probability, the OP of decoding x_n at N and x_s at S can be expressed, respectively, as

$$P_{\text{out}}^N = 1 - \Pr\left[\frac{\omega\mathcal{R}\left(\gamma_N^{x_n}\right)}{2} \geq r_n, \frac{\omega\mathcal{R}\left(\gamma_N^{x_f}\right)}{2} \geq r_f\right], \quad (16)$$

$$P_{\text{out}}^S = 1 - \Pr\left[\frac{\mathcal{R}\left(\gamma_S^{\bar{x}_f}\right)}{2} \geq r_f, \frac{\mathcal{R}\left(\gamma_S^{x_s}\right)}{2} \geq r_s\right]. \quad (17)$$

Further, the outage event at F to decode x_f is determined by two cases. First, when N fails to decode x_f, the outage event at F relies on $\gamma_F^{x_f}$. Second, when N successfully decodes x_f, the outage event depends on γ_F^{e2e}. Considering the probability at which N completes its decoding procedure, the outage event at F is determined by

$$P_{\text{out}}^F = \Pr\left[\frac{\omega\mathcal{R}\left(\gamma_N^{x_n}\right)}{2} \geq r_n, \frac{\mathcal{R}\left(\gamma_F^{\text{e2e}}\right)}{2} < r_f\right] + \Pr\left[\frac{\omega\mathcal{R}\left(\gamma_N^{x_n}\right)}{2} < r_n, \frac{\mathcal{R}\left(\gamma_F^{x_f}\right)}{2} < r_f\right]. \quad (18)$$

III. PERFORMANCE ANALYSIS

A. ANALYSIS OF THE CASCADED CHANNEL DISTRIBUTION

Let us consider $X_s \triangleq \mathbf{h}_{SR}^T \Phi^s \mathbf{h}_{RW}$, $Y_n \triangleq \mathbf{h}_{NR}^T \Phi^n \mathbf{h}_{RS}$, and $Z_f \triangleq h_{NF} + \mathbf{h}_{NR}^T \Phi^f \mathbf{h}_{RF}$. Through statistical tools, the CDFs and PDFs of $|X_s|^2$, $|Y_n|^2$, and $|Z_f|^2$ can be mapped into Gamma distribution (See Appendix A) as

$$F_{|X_s|^2}(x) = 1 - \Gamma(\kappa_s, x/\lambda_s)/\Gamma(\kappa_s), \quad (19)$$

$$f_{|X_s|^2}(x) = \frac{x^{\kappa_s - 1}}{\Gamma(\kappa_s)(\lambda_s)^{\kappa_s}} \exp(-x/\lambda_s), \quad (20)$$

$$F_{|Y_n|^2}(x) = F_{X_n}(y), f_{|Y_n|^2}(x) = f_{|X_n|^2}(y), \quad (21)$$

$$F_{|Z_f|^2}(x) = 1 - \Gamma(\tau_f, x/\theta_f)/\Gamma(\tau_f), \quad (22)$$

$$f_{|Z_f|^2}(x) = \frac{x^{\tau_f - 1}}{\Gamma(\tau_f)(\theta_f)^{\tau_f}} \exp(-x/\theta_f), \quad (23)$$

where $\kappa_s, \lambda_s, \tau_f$, and θ_f are shown in (24)–(26), shown at the bottom of the next page, respectively, with $A_W^s \triangleq \sqrt{\eta_k^s \Omega_{SR}\Omega_{RW}}$ and $B_F^f \triangleq \sqrt{\eta_k^f \Omega_{NR}\Omega_{RF}}$.

It is worth noting that the above CDFs and PDFs that are mapped by $|X_s|^2$, $|Y_n|^2$, and $|Z_f|^2$ into Gamma distributions are general solutions and are still applicable for Rician or Nakagami-m fading by only replacing the moments of variables $|[\mathbf{g}_{SR}]_k|$, $|[\mathbf{g}_{RW}]_k|$, $|[\mathbf{g}_{NR}]_k|$, and $|[g_{NF}]|$. These fundamentals can be found in [56, Ch. 2.2.1].

To guide the right choice for practical implementation, it is worthy to explore the STAR-RIS behavior.

Lemma 1: Given that the number of STAR-RIS elements K is large enough, one can deduce from (24) and (26) that

$$\kappa_s \overset{K\to\infty}{\simeq} \frac{(K-1)^2}{2(2K+1)\left(2^{-2q+4}-\sin^2\left(2^{-q}\pi\right)\right)}, \tag{27}$$

$$\lambda_s \overset{K\to\infty}{\simeq} \frac{2K\left(A_W^s\right)^2\left(1-\sin^2\left(2^{-q}\pi\right)\right)(2K+1)}{2^{-2q+4}(K-1)}, \tag{28}$$

$$\tau_f \overset{K\to\infty}{\simeq} \frac{(K-1)^2\sin^2\left(2^{-q}\pi\right)}{2(2K-1)\left(2^{-2q+4}-\sin^2\left(2^{-q}\pi\right)\right)}, \tag{29}$$

$$\theta_f \overset{K\to\infty}{\simeq} \frac{2K\left(B_F^f\right)^2(2K-1)}{(K-1)}\left(1-\frac{\sin^2\left(2^{-q}\pi\right)}{2^{-2q+4}}\right). \tag{30}$$

From Lemma 1, one can see that the characteristics of the shape components are primarily dominated by K and q, while those of scale components include K, q, and scale parameters of channels A_W^s and B_F^f. Clearly, when q, A_W^s, and B_F^f are fixed, increasing K increases the shape and scale components, improving consequently the envelope of the cascaded channel distribution at the receiving nodes.

Lemma 2: Given that the number of control bits q is large sufficiently (i.e., $q\to\infty$), one has that $2^{-q}\to 0$; thus, $\sin\left(2^{-q}\pi\right)\to 2^{-2q}\pi^2$. From (24) and (26), one can achieve

$$\kappa_s \overset{q\to\infty}{\to} \frac{\left(1+(K-1)\frac{\pi^2}{16}\right)^2}{2\left(1-\frac{\pi^2}{16}\right)\left(1+(2K+1)\frac{\pi^2}{16}\right)}, \tag{31}$$

$$\lambda_s \overset{q\to\infty}{\to} \frac{2K\left(A_W^s\right)^2\left(1-\frac{\pi^2}{16}\right)\left(1+(2K+1)\frac{\pi^2}{16}\right)}{\left(1+(K-1)\frac{\pi^2}{16}\right)}, \tag{32}$$

$$\tau_f \overset{q\to\infty}{\simeq} \frac{\left(\frac{\pi}{4}\sqrt{\Omega_{NF}\pi}+(K-1)B_F^f\frac{\pi^2}{16}+B_F^f+\frac{\Omega_{NF}}{KB_F^f}\right)^2}{\left[\begin{array}{l}2B_F^f\left(\sqrt{\Omega_{NF}\pi}\frac{\pi}{2}+(2K-1)B_F^f\frac{\pi^2}{16}+B_F^f\right.\\ \left.+\frac{\Omega_{NF}}{KB_F^f}\left(1+\frac{\pi}{4}\right)\right)\left(1-\frac{\pi^2}{16}+\frac{\Omega_{NF}}{K\left(B_F^f\right)^2}\left(1-\frac{\pi}{4}\right)\right)\end{array}\right]}, \tag{33}$$

$$\theta_f \overset{q\to\infty}{\simeq} \frac{2K\left(B_F^f\right)^2\left(1-\frac{\pi^2}{16}+\frac{\Omega_{NF}}{K\left(B_F^f\right)^2}\left(1-\frac{\pi}{4}\right)\right)}{\left(\frac{\pi}{4}\sqrt{\Omega_{NF}\pi}+(K-1)B_F^f\frac{\pi^2}{16}+B_F^f+\frac{\Omega_{NF}}{KB_F^f}\right)}\left(\frac{\pi\sqrt{\Omega_{NF}\pi}}{2}+(2K-1)\frac{B_F^f\pi^2}{16}+B_F^f+\Omega_{NF}\frac{\left(1+\frac{\pi}{4}\right)}{KB_F^f}\right). \tag{34}$$

Lemma 2 shows that the shape and scale components converge to a constant value which is determined by the key parameters: K, A_W^s, B_F^f, and Ω_{NF}. From the derived asymptotic expressions, one can readily capture the optimal envelope of the cascaded channel distribution at the receiving nodes under optimal phase-shift configuration in [32], [35], [36]. Thus, one can determine the required number of control bits without performing optimal analysis or simulation.

Since the proposed approaches do not involve any square root in terms of CDFs and PDFs as in [17], [18], it becomes particularly effective in simplifying the system analysis.

B. OUTAGE PERFORMANCE ANALYSIS

1) OP ANALYSIS AT N

On the foundation of (16), closed-form expressions for the OP of N are derived in the following theorem.

Theorem 1: Assuming that $a(\ell_f+1)-\ell_f>0$ and $1-a-\Xi_N a\ell_n>0$ are legitimate, the closed-form OP expression of decoding x_n at N can be represented as

$$P_{\text{out}}^N = 1-\frac{1}{\Gamma(\kappa_n)}\Gamma\left(\kappa_n,\frac{\max\{\delta_f,\delta_n\}}{\lambda_n\varkappa\rho}\right), \tag{35}$$

where $\varkappa=1$ and $\varkappa=1-\beta$ apply to SWIPT-TS and SWIPT-PS, respectively, $\delta_f \triangleq \frac{\ell_f}{a(\ell_f+1)-\ell_f}$ and $\delta_n \triangleq \frac{\ell_n}{1-a-\Xi_N a\ell_n}$ with $\ell_f \triangleq 2^{2r_f/\omega}-1$ and $\ell_n \triangleq 2^{2r_n/\omega}-1$, and $\rho \triangleq P_S/\sigma^2$.

Proof: See Appendix B-A. ■

Theorem 1 indicates that the OP of N in (35) is indeed a function of the key distribution parameters, including the threshold rates r_n and r_f, the TS/PS coefficient α/β, the imperfect SIC indicator Ξ_N, the SNR value ρ, the PA factor a, the number of RIS elements K, the number of control

$$\kappa_s = \frac{\left(1+(K-1)\frac{\sin^2\left(2^{-q}\pi\right)}{2^{-2q+4}}\right)^2}{2\left(1-\frac{\sin^2\left(2^{-q}\pi\right)}{2^{-2q+4}}\right)\left(1+(2K+1)\frac{\sin^2\left(2^{-q}\pi\right)}{2^{-2q+4}}\right)}, \lambda_s = \frac{2K\left(A_W^s\right)^2\left(1-\frac{\sin^2\left(2^{-q}\pi\right)}{2^{-2q+4}}\right)\left(1+(2K+1)\frac{\sin^2\left(2^{-q}\pi\right)}{2^{-2q+4}}\right)}{\left(1+(K-1)\frac{\sin^2\left(2^{-q}\pi\right)}{2^{-2q+4}}\right)}, \tag{24}$$

$$\tau_f = \frac{\left(\frac{\sin\left(2^{-q}\pi\right)}{2^{-q+2}}\sqrt{\Omega_{NF}\pi}+(K-1)B_F^f\frac{\sin^2\left(2^{-q}\pi\right)}{2^{-2q+4}}+B_F^f+\frac{\Omega_{NF}}{KB_F^f}\right)^2}{2\left(B_F^f\left(1-\frac{\sin^2\left(2^{-q}\pi\right)}{2^{-2q+4}}\right)+\frac{\Omega_{NF}}{KB_F^f}\left(1-\frac{\pi}{4}\right)\right)\left(\sqrt{\Omega_{NF}\pi}\frac{\sin\left(2^{-q}\pi\right)}{2^{-q+1}}+(2K-1)B_F^f\frac{\sin^2\left(2^{-q}\pi\right)}{2^{-2q+4}}+B_F^f+\frac{\Omega_{NF}}{KB_F^f}\left(1+\frac{\pi}{4}\right)\right)}, \tag{25}$$

$$\theta_f = \frac{2K\left(B_F^f\right)^2\left(1-\frac{\sin^2\left(2^{-q}\pi\right)}{2^{-2q+4}}+\frac{\Omega_{NF}}{K\left(B_F^f\right)^2}\left(1-\frac{\pi}{4}\right)\right)\left(\sqrt{\Omega_{NF}\pi}\frac{\sin\left(2^{-q}\pi\right)}{2^{-q+1}}+(2K-1)B_F^f\frac{\sin^2\left(2^{-q}\pi\right)}{2^{-2q+4}}+B_F^f+\frac{\Omega_{NF}}{KB_F^f}\left(1+\frac{\pi}{4}\right)\right)}{\frac{\sin\left(2^{-q}\pi\right)}{2^{-q+2}}\sqrt{\Omega_{NF}\pi}+(K-1)B_F^f\frac{\sin^2\left(2^{-q}\pi\right)}{2^{-2q+4}}+B_F^f+\frac{\Omega_{NF}}{KB_F^f}}. \tag{26}$$

bits q, the ES coefficient η_k, and scale fading parameters of $S-R$ and $R-N$ links. From (35), one can recognize that:

- For network requirements, when $r_f > r_n$, the OP of N is independent of r_f. Thus, when r_n decreases (i.e., ℓ_f reduces), the OP of N improves, which is in accordance with the fact that the lower data rate reduces the chances of outages. However, when $r_f < r_n$, the OP of N is highly dominated by r_f. In particular, the higher the data rate r_f, the higher decoding errors of x_f occur, which increases the OP of N.
- For SWIPT, in the TS case, as α increases, the factor ℓ_f increases, while for the PS case, the factor $\varkappa$ reduces with the increase of β. These shed light on the fact that there is a performance trade-off between the energy harvesting process and data transmission. In particular, the more energy is harvested, the more data transmission is degraded, leading to a reduction in the OP of N in the first stage. In return, the performance quality of both S and F is enhanced in the second stage.
- For SIC process, it is clear that for given $r_f = r_n$, when Ξ_N increases, the value of $1-a-\Xi_N a\ell_n$ becomes smaller, which means that $1/[a(\ell_f+1)-\ell_f] < 1/[1-a-\Xi_N a\ell_n]$. This results in an increase in the OP of N. Therefore, there is a need for the quality improvement of SIC design to achieve better outage performance.
- For SNR settings, when ρ increases, the OP of N consequently decreases, which reflects the fact that outage events reduce with the higher transmit power P. Interestingly, increasing ρ to infinite ($1/\rho \to 0$), the OP tends to zero due to $\Gamma(\kappa_n, 0) = \Gamma(\kappa_n)$.
- For power allocation, it is pointed out from (24) that there exists a PA trade-off to the OP of N. More precisely, when $\max\{\delta_f, \delta_n\} = \delta_f$, increasing a decreases the OP of N due to decrease in δ_f. In contrast, the OP of N is improved due to the increase in δ_n.

Corollary 1: At high SNR (i.e., $\rho \to \infty$), considering the first-order series representation in [52, eq. (8.354.2)], the OP of decoding x_n at N in (35) can be simplified as

$$P_{\text{out}}^{N,\infty} \simeq \frac{1}{\Gamma(\kappa_n+1)}\left(\frac{\max\{\delta_f, \delta_n\}}{\lambda_n \varkappa \rho}\right)^{\kappa_n}. \tag{36}$$

Remark 1: The above results show that $P_{\text{out}}^{N,\infty} \propto 1/\rho^{\kappa_n}$. Therefore, the diversity gain of κ_n can be achieved at N. Herein, one can recognize that the characteristic of diversity gain depends on two properties of STAR-RIS designs: on the one hand, it suffers from the number of STAR-RIS elements K and, on the other hand, it is dominated by the number of control bits q, which can be found in Lemmas 1 and 2.

2) OP ANALYSIS AT S

From the outage event formulated in (17), the accurate OP of F can be evaluated in the following theorem.

Theorem 2: Knowing that $b(\bar{\ell}_f+1)-\bar{\ell}_f > 0$ and $1-a-\Xi_S b\bar{\ell}_n > 0$, a closed-form OP expression of decoding x_s at S can be derived as

$$P_{\text{out}}^{S} = 1 - \frac{1}{\Gamma(\kappa_n)^2} G_{1,3}^{3,0}\left(\frac{\max\{\bar{\delta}_f, \bar{\delta}_n\}}{\nu\lambda_n^2\rho}\Big|_{\kappa_n, \kappa_n, 0}^{1}\right), \tag{37}$$

where $\bar{\delta}_f \triangleq \frac{\bar{\ell}_f}{b(\bar{\ell}_f+1)-\bar{\ell}_f}$ and $\bar{\delta}_n \triangleq \frac{\bar{\ell}_n}{1-b-\Xi_S b\bar{\ell}_n}$ with $\bar{\ell}_f \triangleq 2^{2r_f}-1$ and $\bar{\ell}_n \triangleq 2^{2r_s}-1$. If SWIPT-TS is adopted, $\nu = \zeta\alpha$, otherwise, $\nu = \zeta\beta$.

Proof: See Appendix B-B. ∎

As observed in Theorem 2, the OP of S is a function of r_s, r_f, the TS/PS coefficient α/β, the energy conversion efficiency ζ, the imperfect SIC indicator Ξ_S, the SNR value ρ, the PA factor b, the number of antennas N, the number of control bits q, the ES coefficient η_k, and scale fading parameters $S-R$ links and $R-N$ links. Some useful insights from Theorem 2 can be drawn as follows:

- The larger the transmit power (i.e., when ρ increases), the lower the OP of S incurs.
- When $r_s < r_f$, decreasing r_s improves the OP of S. Inversely, the OP of S increases with increasing r_f.
- When the SIC imperfection levels increase, the OP of S also increases.
- Improving the energy harvesting capabilities α/β (or for increased energy conversion efficiency factor ζ), the OP of S also improves.

Corollary 2: By applying the series representation in [52, eq. (9.33.1)], P_{out}^{S} in (37) can be further simplified as

$$P_{\text{out}}^{S,\infty} \simeq \frac{1}{\Gamma(\kappa_n)^2 \rho^{\kappa_n}(\nu\lambda_n^2)^{\kappa_n}} \sum_{m=0}^{\infty} \frac{1}{m!}(1-\kappa_n)^m \times G_{1,3}^{3,0}\left(\max\{\bar{\delta}_f, \bar{\delta}_n\}\Big|_{\kappa_n+m, \kappa_n, 0}^{1}\right). \tag{38}$$

Remark 2: Obviously, $P_{\text{out}}^{S,\infty} \propto 1/\rho^{\kappa_n}$, which concludes that the diversity gain of κ_n can be achieved at S.

3) OP ANALYSIS AT F

From the outage event in (18), the OP expression of F can be presented in the following theorem.

Theorem 3: The closed-form expression for the OP of F can be written as

$$P_{\text{out}}^{F} = \begin{cases} \Delta_1\Delta_2, & \ell_f < \frac{a}{1-a} \wedge \bar{\ell}_f < \frac{a}{1-a} \wedge \bar{\ell}_f < \frac{b}{1-b}, \\ \Delta_1, & \ell_f > \frac{a}{1-a} \wedge \bar{\ell}_f < \frac{a}{1-a} \vee \bar{\ell}_f < \frac{b}{1-b}, \\ 1, & \ell_f > \frac{a}{1-a} \wedge \bar{\ell}_f > \frac{a}{1-a} \wedge \bar{\ell}_f > \frac{b}{1-b}, \end{cases} \tag{39}$$

where

$$\Delta_1 = 1 - \frac{1}{\Gamma(\kappa_f)}\Gamma\left(\kappa_f, \frac{\hat{\delta}_f}{\lambda_f\rho}\right),$$

$$\Delta_2 = 1 - \frac{1}{\Gamma(\kappa_n)\Gamma(\tau_f)} G_{1,3}^{3,0}\left(\frac{\bar{\delta}_f}{\nu\theta_f\lambda_n\rho}\Big|_{\kappa_n, \tau_f, 0}^{1}\right) + \frac{1}{\Gamma(\tau_f)} \sum_{l=1}^{L} \frac{\pi\delta_f\sqrt{1-\chi_l^2}\psi_l^{\kappa_n-1}}{2L\Gamma(\kappa_n)\varkappa\rho\lambda_n^{\kappa_n}} \exp(-\psi_l/\lambda_n)\Gamma\left(\tau_f, \frac{\bar{\delta}_f}{\theta_f\rho\nu\psi_l}\right),$$

with $\hat{\delta}_f \triangleq \frac{\bar{\ell}_f}{a(\bar{\ell}_f+1)-\bar{\ell}_f}$, $\chi_l = \cos((2l-1)\pi/2/L)$, $\psi_l = \delta_f/\varkappa\rho(\chi_l+1)/2$, and L being the accuracy trade-off factor.

Proof: See Appendix B-C. ∎

Since the OP form of F in Theorem 3 seems quite difficult to infer the key impact of crucial parameters on its outage behavior, it is worthy to explore whether there are any alternative solutions to derive OP in a simpler manner.

Theorem 4: Suppose that N always detects x_f successfully in the first stage, the outage at F only happens if $\max\{\gamma_F^{x_f}, \gamma_F^{\tilde{x}_f}\} < \bar{\ell}_f$, yielding the lower bound OP

$$P_{\text{out}}^{F} = F_{|X_f|^2}\left(\frac{\bar{\delta}_f}{\rho}\right)\int_0^{\infty} F_{|X_n|^2}\left(\frac{\bar{\delta}_f}{\nu\rho z}\right) f_{|Z_f|^2}(z)dz$$
$$= \left[1 - \frac{1}{\Gamma(\kappa_f)}\Gamma\left(\kappa_f, \frac{\bar{\delta}_f}{\lambda_f\rho}\right)\right]$$
$$\left[1 - \frac{1}{\Gamma(\kappa_n)\Gamma(\tau_f)} G_{1,3}^{3,0}\left(\frac{\bar{\delta}_f/\theta_f}{\nu\lambda_n\rho}\middle|\begin{matrix}1\\ \tau_f, \kappa_n, 0\end{matrix}\right)\right]. \quad (40)$$

At high SNR (i.e., $\rho \to \infty$), by applying the first-order series representation in [52, eqs. (8.354.2) and (9.33.3)], the OP of F in (40) can be asymptotically simplified as

$$P_{\text{out}}^{F,\infty} \simeq \frac{\left(\bar{\delta}_f/\lambda_f\right)^{\kappa_f}}{\Gamma(\kappa_f+1)\rho^{\kappa_f}} \frac{1/\left(\nu\lambda_n\theta_f\right)^{\tau_f}}{\Gamma(\kappa_n)\Gamma(\tau_f)\rho^{\tau_f}} \sum_{m=0}^{\infty}\frac{(1-\kappa_n)^m}{m!}$$
$$G_{1,3}^{3,0}\left(\bar{\delta}_f\middle|\begin{matrix}1\\ \tau_f+m, \kappa_n, 0\end{matrix}\right). \quad (41)$$

As can be seen in (41), the OP of F is improved with an increase of ρ, r_f, harvesting energy coefficients (i.e., α/β), as well as the improved energy conversion efficiency.

Theorem 5: Consider the hypothesis that N always fails to detect x_f in the first stage, the OP of F only happens if $\gamma_F^{x_f} < \bar{\ell}_f$. Thus, the upper bound OP of F is given by

$$P_{\text{out}}^{F} \simeq \Pr\left[\gamma_F^{x_f} < \hat{\delta}_f\right] = 1 - \frac{1}{\Gamma(\kappa_f)}\Gamma\left(\kappa_f, \frac{\hat{\delta}_f}{\lambda_f\rho}\right). \quad (42)$$

At high SNR regime, using the first-order series representation in [52, eq. (8.354.2)], the OP of F in (42) can be asymptotically simplified as

$$P_{\text{out}}^{F,\infty} \simeq \left(\hat{\delta}_f/\lambda_f\right)^{\kappa_f} / \left[\Gamma(\kappa_f+1)\rho^{\kappa_f}\right]. \quad (43)$$

Remark 3: The results in (41) and (43) confirm that the diversity order of F is either κ_f or $(\tau_f + \kappa_f)$.

C. EFFECTIVE ERGODIC CAPACITY ANALYSIS

1) EFFECTIVE ERGODIC CAPACITY AT N

With the knowledge of the threshold rates r_f and r_n and the received power distribution at N, the effective EC of N can be rewritten from (13) as

$$\bar{\mathcal{R}}_N = \frac{\omega}{2}\mathrm{E}\left\{\log_2\left(1+\frac{(1-a)\varkappa\rho|X_n|^2}{a\Xi_N\varkappa\rho|X_n|^2+1}\right)\right\}\Pr\left[|X_n|^2 \geq \frac{\delta_f}{\varkappa\rho}\right]$$
$$= \frac{\omega}{2\ln 2}\int_0^{\infty}\ln\left(\frac{1+(1-a+a\Xi_N)\varkappa\rho x}{1+a\Xi_N\varkappa\rho x}\right) f_{|X_n|^2}(x)dx$$
$$\times\left[1 - F_{|X_n|^2}\left(\frac{\delta_f}{\varkappa\rho}\right)\right]. \quad (44)$$

Making the use of identities $\ln(\frac{1+x}{1+y}) = \ln(1+x) - \ln(1+y)$ and $\ln(z+1) = G_{2,2}^{1,2}(z|\begin{smallmatrix}1,1\\1,0\end{smallmatrix})$ and then plugging $f_{|X_n|^2}(\cdot)$ and $F_{|X_n|^2}(\cdot)$ into the above, one can get the following proposition, thanks to [52, eq. (7.813.1)].

Proposition 1: An exact closed-form expression for the effective EC at N can be derived as

$$\bar{\mathcal{R}}_N = \frac{\omega}{2\ln 2}\left[G_{3,2}^{1,3}\left((1-a+a\Xi_N)\lambda_n\varkappa\rho\middle|\begin{matrix}1-\kappa_n, 1, 1\\ 1, 0\end{matrix}\right)\right.$$
$$\left. - G_{3,2}^{1,3}\left(a\Xi_N\lambda_n\varkappa\rho\middle|\begin{matrix}1-\kappa_n, 1, 1\\ 1, 0\end{matrix}\right)\right]\frac{\Gamma\left(\kappa_n, \frac{\delta_f}{\varkappa\lambda_n\rho}\right)}{\Gamma(\kappa_n)\Gamma(\kappa_n)}. \quad (45)$$

At high SNR regime, i.e., $\rho \to \infty$, making use of the fact that $x+1 \simeq x$ as $x \to \infty$ and the first-order series representation in [52, eq. (8.354.2)] for small x, the effective EC at N in (43) can be asymptotically approximated as

$$\bar{\mathcal{R}}_N^{\infty} = \frac{\omega}{2}\{\log_2\left(1+\frac{1-a}{a\Xi_N}\right)\Pr\left[|X_n|^2 \geq \frac{\delta_f}{\varkappa\rho}\middle|\rho\to\infty\right]$$
$$= \frac{\omega}{2}\log_2\left(1+\frac{1-a}{a\Xi_N}\right)\left[1 - \frac{\left(\delta_f/[\varkappa\lambda_n\rho]\right)^{\kappa_n}}{\Gamma(\kappa_n+1)}\right]. \quad (46)$$

The above expression reveals that:

- The longer the splitting time α (i.e., $\omega = 1-\alpha$) or the larger the splitting signal portion β (i.e., $\varkappa = 1-\beta$) for the EH process, the lower the effective EC incurs.
- The larger the transmit power (i.e., ρ), the higher the effective EC; however, when $\rho \simeq \infty$, the effective EC saturates.
- The larger the PA factor a, the smaller the effective EC.
- The higher the residual SIC level Ξ_N, the smaller the effective EC.

2) EFFECTIVE ERGODIC CAPACITY AT S

From (14), the effective EC of S can be rearranged as

$$\bar{\mathcal{R}}_S = \frac{1}{2}\mathrm{E}\left\{\log_2\left(1+\frac{(1-b)\nu\rho|X_n|^2|Y_n|^2}{b\Xi_S\nu\rho|X_n|^2|Y_n|^2+1}\right)\right\}$$
$$\times\Pr\left[|X_n|^2|Y_n|^2 \geq \frac{\bar{\delta}_f}{\nu\rho}\right]$$
$$= \frac{1}{2\ln 2}\underbrace{\int_0^{\infty}\ln\left(1+\frac{(1-b)\nu\rho x}{1+b\Xi_S\nu\rho x}\right) f_{|X_n|^2|Y_n|^2}(x)dx}_{I_1}$$
$$\times\underbrace{\int_0^{\infty}\left[1 - F_{|Y_n|^2}\left(\frac{\bar{\delta}_f}{x\nu\rho}\right)\right] f_{|X_n|^2}(x)dx}_{I_2}. \quad (47)$$

To solve (47), we consider the following PDF

$$f_{|X_n|^2|Y_n|^2}(z)dx = \int_0^{\infty} f_{|X_n|^2}(x)dx f_{|Y_n|^2}(z/x)\frac{1}{x}dx$$
$$= \frac{z^{\kappa_n-1}}{\Gamma(\kappa_n)^2\left(\lambda_n\right)^{2\kappa_n}} 2\mathcal{K}_0\left(2\sqrt{z/\lambda_n^2}\right). \quad (48)$$

Using [52, eq. (3.471.9)], I_1 in (47) can be reformulated as

$$I_1 = 2\int_0^\infty \ln\left(1+\frac{(1-b)\nu\rho x}{1+b\Xi_S\nu\rho x}\right)\frac{x^{\kappa_n-1}\mathcal{K}_0\left(2\sqrt{\frac{x}{\lambda_n^2}}\right)dx}{\Gamma(\kappa_n)^2(\lambda_n)^{2\kappa_n}}$$
$$= 2\int_0^\infty \ln\left(1+\frac{(1-b)\nu\rho\lambda_n^2 z}{1+b\Xi_S\nu\rho\lambda_n^2 z}\right)\frac{z^{\kappa_n-1}\mathcal{K}_0\left(2\sqrt{z}\right)}{\Gamma(\kappa_n)^2}dz. \quad (49)$$

Meanwhile, I_2 in (47) can be rewritten as

$$I_2 = \int_0^\infty \Gamma\left(\kappa_n, \frac{\bar{\delta}_f}{x\lambda_n\nu\rho}\right)\frac{x^{\kappa_n-1}\exp\left(-\frac{x}{\lambda_n}\right)}{\Gamma(\kappa_n)^2\lambda_n^{\kappa_n}}dx. \quad (50)$$

Following the identities $\ln(\frac{1+x}{1+y}) = \ln(1+x)-\ln(1+y)$ and $\ln(z+1) = G_{2,2}^{1,2}(z|\,{}^{1,1}_{1,0})$ and invoking [52, eqs. (7.821.3) and (9.31.2)], one can attain the solution for I_1, whereas I_2 can be solved using the same derivation as in (B.2). After some algebraic steps, one can get the following proposition.

Proposition 2: An exact closed-form effective EC expression for S can be derived as

$$\bar{\mathcal{R}}_S = \frac{1/[2\ln 2]}{\Gamma(\kappa_n)^4}\left[G_{2,4}^{4,1}\left(\frac{1/[\lambda_n^2\nu\rho]}{1-b+b\Xi_S}\Big|\begin{matrix}0,1\\ \kappa_n,\kappa_n,0,0\end{matrix}\right)\right.$$
$$\left. - G_{2,4}^{4,1}\left(\frac{1}{b\Xi_S\lambda_n^2\nu\rho}\Big|\begin{matrix}0,1\\ \kappa_n,\kappa_n,0,0\end{matrix}\right)\right]G_{1,3}^{3,0}\left(\frac{\bar{\delta}_f}{\nu\lambda_n^2\rho}\Big|\begin{matrix}1\\ \kappa_n,\kappa_n,0\end{matrix}\right). \quad (51)$$

At high SNR regime, i.e., $\rho\to\infty$, using the approximation $x+1\simeq x$ as $x\to\infty$, the equivalent outcome $|X_n|^2|Y_n|^2\simeq|X_n|^4$ (this is because channels from the source to the near user and vice versa do not differ too much), and the first-order series representation in [52, eq. (8.354.2)] for small x, the effective EC at S in (47) can be asymptotically approximated as

$$\bar{\mathcal{R}}_S = \frac{1}{2}\log_2\left(1+\frac{1-b}{b\Xi_S}\right)\Pr\left[|X_n|^2\geq\sqrt{\frac{\bar{\delta}_f}{\nu\rho}}\Big|\rho\to\infty\right]$$
$$= \frac{1}{2}\log_2\left(1+\frac{1-b}{b\Xi_S}\right)\left[1-\frac{\left(\bar{\delta}_f/[\lambda_n\nu\rho]\right)^{\kappa_n/2}}{\Gamma(\kappa_n+1)}\right]. \quad (52)$$

The outcome in (52) points out that:

- The longer the splitting time α or the larger the splitting signal portion β or the energy conversion efficiency ζ, the smaller the effective EC of S.
- The effective EC of S improves in low and moderate SNR regimes but saturates at high SNR regime, which can be verified by considering $\rho\simeq 0$.
- As the remaining residual interference Ξ_S increases, the effective EC decreases.
- Allocating a higher power budget for F's signals (i.e., b) reduces the effective EC of S.

3) EFFECTIVE ERGODIC CAPACITY AT F

From (15), the effective EC of F can be rewritten as

$$\bar{\mathcal{R}}_F = \left\{\frac{1}{2}\mathcal{R}\left(\gamma_F^{x_f}\right) : \frac{\omega}{2}\mathcal{R}\left(\gamma_N^{x_f}\right) < r_f\right\}\bigcup$$
$$\left\{\mathcal{R}\left(\gamma_F^{x_f}\right)+\mathcal{R}\left(\gamma_F^{\bar{x}_f}\right)\right.$$
$$\left. - \mathcal{R}\left(\min\left\{\gamma_F^{x_f},\gamma_F^{\bar{x}_f}\right\}\right) : \frac{\omega}{2}\mathcal{R}\left(\gamma_N^{x_f}\right)\geq r_f\right\}$$
$$= \frac{1}{2}\underbrace{\mathrm{E}\left\{\log_2\left(1+\gamma_F^{x_f}\right)\right\}}_{Q_1}+\frac{1}{2}\left[\underbrace{\mathrm{E}\left\{\log_2\left(1+\gamma_F^{\bar{x}_f}\right)\right\}}_{Q_2}\right.$$
$$\left. - \underbrace{\mathrm{E}\left\{\log_2\left(1+\min\{\gamma_F^{x_f},\gamma_F^{\bar{x}_f}\}\right)\right\}}_{Q_3}\right]\left[1-F_{|X_n|^2}\left(\frac{\delta_f}{\varkappa\rho}\right)\right]. \quad (53)$$

Similar to the integral in (44) for Q_1 and the integral in (49) for Q_2, the solutions for Q_1 and Q_2 are given by

$$Q_1 = \mathrm{E}\left\{\log_2\left(1+\frac{a\rho|X_f|^2}{(1-a)\rho|X_f|^2+1}\right)\right\}$$
$$= \frac{1}{\ln 2}\int_0^\infty \ln\left(\frac{1+\rho x}{1+(1-a)\rho x}\right)f_{|X_f|^2}(x)dx$$
$$= \frac{1}{\ln 2\Gamma(\kappa_f)}\left[G_{3,2}^{1,3}\left(\lambda_f\rho\Big|\begin{matrix}1-\kappa_f,1,1\\ 1,0\end{matrix}\right)-\right.$$
$$\left. G_{3,2}^{1,3}\left((1-a)\lambda_f\rho\Big|\begin{matrix}1-\kappa_f,1,1\\ 1,0\end{matrix}\right)\right], \quad (54)$$

$$Q_2 = \mathrm{E}\left\{\log_2\left(1+\frac{b\nu\rho|X_n|^2|Z_f|^2}{(1-b)\nu\rho|X_n|^2|Z_f|^2+1}\right)\right\}$$
$$= \frac{1}{\ln 2}\int_0^\infty \ln\left(\frac{1+\nu\rho z}{1+(1-a)\nu\rho z}\right)f_{|X_n|^2|Z_f|^2}(z)dz$$
$$= \frac{1}{\ln 2\Gamma(\tau_f)\Gamma(\kappa_n)}\left[G_{2,4}^{4,1}\left(\frac{1}{\lambda_n\theta_f\nu\rho}\Big|\begin{matrix}0,1\\ \tau_f,\kappa_n,0,0\end{matrix}\right)\right.$$
$$\left. -G_{2,4}^{4,1}\left(\frac{1}{(1-b)\lambda_n\theta_f\nu\rho}\Big|\begin{matrix}0,1\\ \tau_f,\kappa_n,0,0\end{matrix}\right)\right]. \quad (55)$$

Meanwhile, following a partial-integral-by-part approach [57, eq. (27)], the solution for Q_3 can be given by

$$Q_3 = \frac{1}{\ln 2}\int_0^\infty \frac{1-F_{\gamma_F^{\min}}(x)}{1+x}dx, \quad (56)$$

where the CDF of $\gamma_F^{\min} = \min\{\gamma_F^{x_f},\gamma_F^{\bar{x}_f}\}$ can be derived as

$$F_{\gamma_F^{\min}}(x) = 1-\Pr\left[\gamma_F^{x_f}>x\right]\Pr\left[\gamma_F^{\bar{x}_f}>x\right]$$
$$= 1-\left[1-F_{|X_f|^2}\left(\frac{x}{[a-(1-a)x]\rho}\right)\right]$$
$$\int_0^\infty\left[1-F_{|Z_f|^2}\left(\frac{x/[\nu\rho]}{[b-(1-b)x]y}\right)\right]f_{|X_n|^2}(y)dy$$
$$= 1-\frac{1}{\Gamma(\kappa_f)\Gamma(\kappa_n)\Gamma(\tau_f)}\Gamma\left(\kappa_f,\frac{x/[\lambda_f\rho]}{a-(1-a)x}\right)$$
$$\times G_{1,3}^{3,0}\left(\frac{x/[\nu\theta_f\lambda_n\rho]}{b-(1-b)x}\Big|\begin{matrix}1\\ \kappa_n,\tau_f,0\end{matrix}\right). \quad (57)$$

The above integral can be solved by performing the analysis similar to (B.2). Note that $F_{\gamma_F^{\min}}(x)$ only holds when $x<\min\{a/(1-a),b/(1-b)\}$, otherwise, $F_{\gamma_F^{\min}}(x)=1$.

Accordingly, Q_3 can be rewritten as

$$Q_3 = \frac{1}{\Gamma(\kappa_f)\Gamma(\kappa_n)\Gamma(\tau_f)\ln 2} \int_0^{\min\{\frac{a}{1-a},\frac{b}{1-b}\}} \frac{1}{1+x} \Gamma\left(\kappa_f, \frac{x/[\lambda_f\rho]}{a-(1-a)x}\right) G_{1,3}^{3,0}\left(\frac{x/[\nu\theta_f\lambda_n\rho]}{b-(1-b)x}\Big|_{\kappa_n,\tau_f,0}^{1}\right)dx. \quad (58)$$

The integral of Q_3 is determined by two cases. For case I, taking it for granted that $(a = b)$, yielding $\min\{\frac{a}{1-a}, \frac{b}{1-b}\} = a/(1-a)$. By performing the variable transformation $y = x/[a+(1-a)x]$, Q_3 can be expressed as

$$Q_3^{a=b} = \frac{a}{1-a}\int_0^{\infty} \frac{\Gamma(\kappa_f, \frac{y}{\lambda_f\rho}) G_{1,3}^{3,0}\left(\frac{y/[\nu\theta_f]}{\lambda_n\rho}\Big|_{\kappa_n,\tau_f,0}^{1}\right)}{(y+1)(y+\frac{1}{1-a})}dy$$
$$= \Bigg[G_{1,1:1,2:1,3}^{1,1:2,0:3,0}\left(\begin{matrix}0\\0\end{matrix}\Big|\begin{matrix}1\\\kappa_f,0\end{matrix}\Big|\begin{matrix}1\\\kappa_n,\tau_f,0\end{matrix}\Big|\begin{matrix}\frac{1}{\lambda_f\rho}\\\frac{1}{\nu\theta_f\lambda_n\rho}\end{matrix}\right) - G_{1,1:1,2:1,3}^{1,1:2,0:3,0}\left(\begin{matrix}0\\0\end{matrix}\Big|\begin{matrix}1\\\kappa_f,0\end{matrix}\Big|\begin{matrix}1\\\kappa_n,\tau_f,0\end{matrix}\Big|\begin{matrix}\frac{1}{(1-a)\lambda_f\rho}\\\frac{(\nu\theta_f)^{-1}}{(1-a)\lambda_n\rho}\end{matrix}\right)\Bigg], \quad (59)$$

where the last step is attained by making the following steps: 1) Conducting partial fraction decomposition for $1/(y+1)/(y+1/(1-a)) = (1-a)/a[1/(y+1) - 1/(y+1/(1-a))]$; 2) Carrying out three transformations $(y+1)^{-1} = G_{1,1}^{1,1}(y|\begin{smallmatrix}0\\0\end{smallmatrix})$, $(y+\frac{1}{1-a})^{-1} = (1-a)G_{1,1}^{1,1}((1-a)y|\begin{smallmatrix}0\\0\end{smallmatrix})$, and $\Gamma(\kappa_f, \frac{y}{\lambda_f\rho}) = G_{1,2}^{2,0}(\frac{y}{\lambda_f\rho}|\begin{smallmatrix}1\\\kappa_f,0\end{smallmatrix})$; and 3) Using the identity [58, eq. (07.34.21.0081.01)].

For case II $(a \neq b)$, it is not possible to achieve the exact closed-form solution for Q_3. We tackle such challenges using the Riemann integral approximation method as in [51, eq. (46)] for finite integral approximation, yielding

$$Q_3^{a\neq b} = \frac{2\min\{\frac{a}{1-a},\frac{b}{1-b}\}}{\left(\min\{\frac{a}{1-a},\frac{b}{1-b}\}+2\right)}\Gamma\left(\kappa_f, \frac{\min\{\frac{a}{1-a},\frac{b}{1-b}\}}{2\lambda_f\rho}\right) \times G_{1,3}^{3,0}\left(\frac{\min\{\frac{a}{1-a},\frac{b}{1-b}\}}{2\nu\theta_f\lambda_n}\Big|_{\kappa_n,\tau_f,0}^{1}\right). \quad (60)$$

Proposition 3: Based on the developed above, closed-form approximation expression for the effective EC of F can be derived as

$$\bar{\mathcal{R}}_F = \frac{1}{2}Q_1 + \frac{1}{2}\Big[Q_2 - Q_3\Big]\frac{1}{\Gamma(\kappa_n)}\Gamma\left(\kappa_n, \frac{\delta_f}{\varkappa\lambda_f\rho}\right), \quad (61)$$

where

$$Q_3 = \frac{1}{\Gamma(\kappa_f)\Gamma(\kappa_n)\Gamma(\tau_f)\ln 2}\begin{cases} Q_3^{a=b}, \text{ If } a=b,\\ Q_3^{a\neq b}, \text{ If } a\neq b.\end{cases}$$

At high SNR regime, i.e., $\rho \to \infty$, using the approximation $x+1 \simeq x$ as $x \to \infty$ and the first-order series representation in [52, eq. (8.354.2)] for small x, the effective EC at F in (53) can be asymptotically approximated as

$$\bar{\mathcal{R}}_F = \frac{1}{2}\log_2\left(1+\frac{a}{1-a}\right)\frac{\left(\bar{\delta}_f/[\varkappa\lambda_n\rho]\right)^{\kappa_n}}{\Gamma(\kappa_n+1)} + \frac{1}{2}\log_2\left(1+\max\left\{\frac{a}{1-a},\frac{b}{1-b}\right\}\right)\left[1-\frac{\left(\bar{\delta}_f/[\varkappa\lambda_n\rho]\right)^{\kappa_n}}{\Gamma(\kappa_n+1)}\right]. \quad (62)$$

The obtained EC expression in (62) indicates that:

- When the term $\max\{\frac{a}{1-a}, \frac{b}{1-b}\} = \frac{a}{1-a}$ occurs, the effective EC of S becomes constant, represented by $\frac{1}{2}\log_2(1+\frac{a}{1-a})$. This means that the effective EC is not affected by any distributed system parameter.
- At $\max\{\frac{a}{1-a}, \frac{b}{1-b}\} = \frac{b}{1-b}$, there exists a trade-off between the cooperative communication from N and direct communication from S. This is because increasing the transmit SNR reduces the upper component in (62) but increases the lower component of (62), and a similar clarification can also be found when evaluating α, β, and ζ in the term of ν.

IV. NUMERICAL RESULTS AND DISCUSSIONS

This section presents some illustrative numerical examples and Monte Carlo simulations to corroborate the obtained theorems and propositions in Section III. Considering pathloss propagation, i.e., $\Omega_{\text{TxRx}} = (1+d_{\text{TxRx}}/d_0)^{-\epsilon}$ [43], where d_{TxRx} represents the physical distance between Tx and Rx nodes, d_0 is the reference distance, and ϵ is the pathloss exponent.[4] Without loss of generality, the system is set up as follows: 1) Location in 2D meter-scale: $S(0,0)$, $R(30,30)$, $N(50,0)$, and $F(50,50)$; 2) Reference distance and path loss coefficient: $d_0 = 30$ m and $\epsilon = 3$ [43]; 3) STAR-RIS design: $\{\eta_k^s\}_{k=1}^K = 0.25$ [32], [34]; 4) EH circuit quality: $\zeta = 0.8$ [57]; and 5) Accuracy trade-off parameter: $L = 10$.

A. VALIDATION OF THE CASCADED CHANNEL DISTRIBUTION

Section III-A provides the CDFs and PDFs of $|X_s|^2$, $|Y_n|^2$, and $|Z_f|^2$ in Eqs. (19)-(23). The derivations of these CDFs and PDFs are obtained based on the moment-matching approach. In order to validate these, Fig. 2 illustrates the simulated CDFs and PDFs of $|X_s|^2$, $|Y_n|^2$, and $|Z_f|^2$ and compares them against the corresponding analytical expressions. In Fig. 2(a), it is observed that when q is small, the analytical CDFs slightly deviate from the simulated CDFs. In contrast, when q becomes larger, the CDFs improve. This is because using control bits q can help mitigate the impact of residual error phases, leading to great agreement between the analytical CDFs and the simulated ones. Also, we can see that the analytical CDF for the case of $q = 4$ approaches the case of $q = \infty$ (known as perfect phase-shift alignment [32], [35], [36]) and the gap is quite small. This means that using more than 4-bit control does not yield much more channel gain improvement. Next, in Fig. 2(b), we quantify the analytical PDFs with the simulated CDFs. From the figure, it is clear that the developed PDFs with $q = 4$ provide comparative accuracy with the simulated PDFs.

4. Note that since the developed expressions are a unique function of users' distance that are static within each certain time interval and can be known via feedback CSI procedure, it is possible to reproduce the performance of the considered system by changing the input of distance parameters according to the rapid change of the user's position without any challenges.

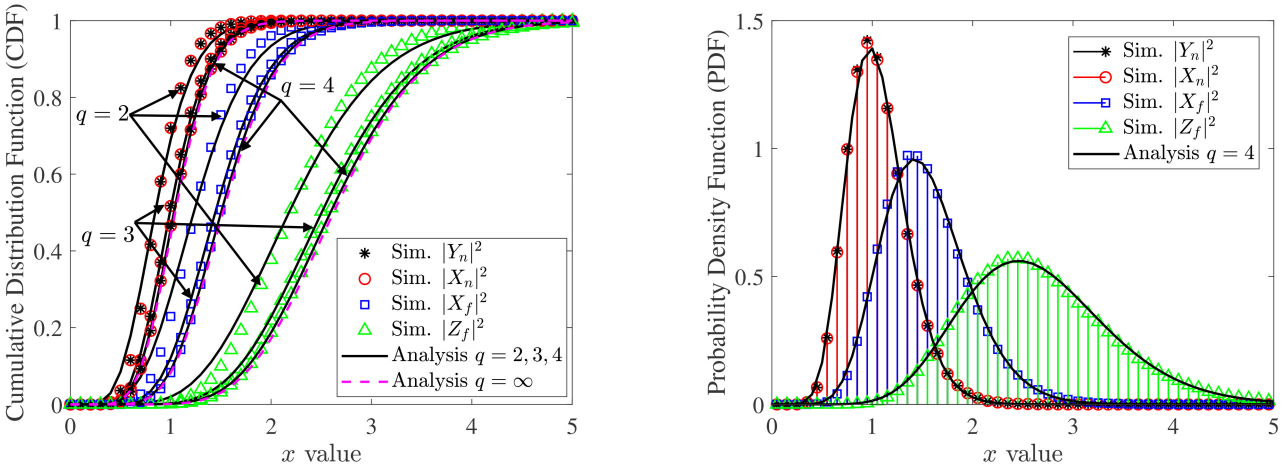

(a) CDF validation. (b) PDF validation.

FIGURE 2. Illustration of the developed CDFs and PDFs in Eqs. (19) –(23) by assuming $K = 32$.

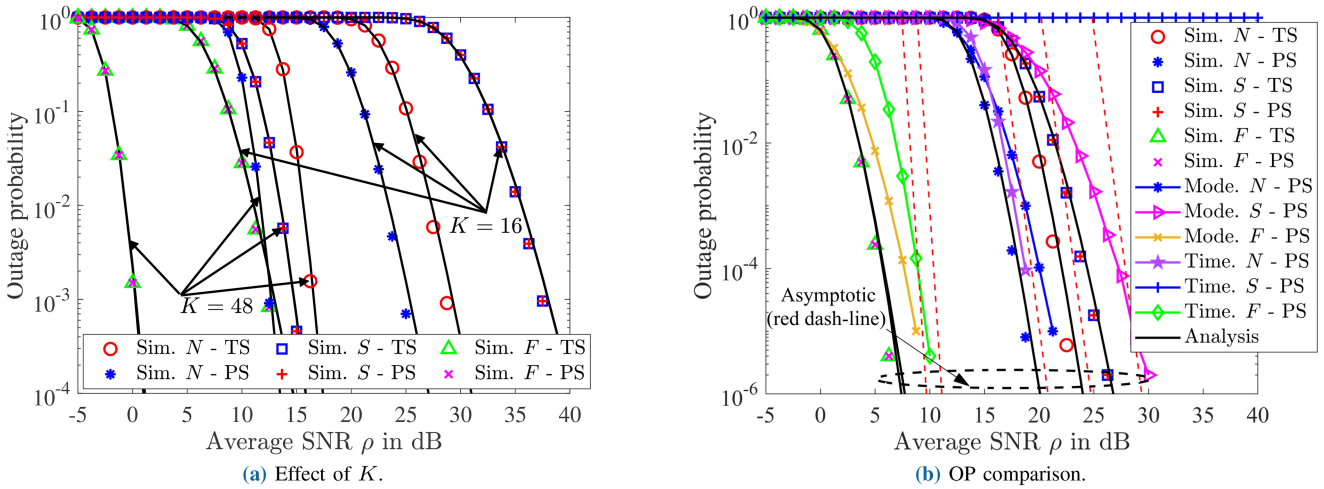

(a) Effect of K. (b) OP comparison.

FIGURE 3. OP versus SNR: a) Effect of K and b) OP comparison with different STAR-RIS protocols.

B. OUTAGE PERFORMANCE EVALUATION

Fig. 3 plots the OPs of N, S, and F as a function of transmit SNR ρ under varying STAR-RIS element settings, where the numerical results are produced by setting $a = 0.8$, $b = 0.6$, $\Psi_N = \Psi_S = 0.01$, $\alpha = \beta = 0.5$, $q = 4$, $r_f = 0.5$, $r_n = 0.75$ bps/Hz, and $r_s = 1.5$ bps/Hz. It is observed from the figure that the analytical outcomes (solid lines) show good approximation with the simulation results (markers). It is also seen from Fig. 3(a) that the OP improves with the increase in the transmit SNR and quickly converges to zero at high SNR regime. This means that the higher the transmitted SNR, the higher the reliability of the transmission. In addition, the results also indicate that the OP decreases with increasing K. In particular, when increasing K from 16 to 48, the system can save over the transmit SNR up to 10 dB with N and F while reaching out 20 dB of transmit SNR with S. This sheds light on the fact that increasing K can not only improve the reliability of transmission but also efficiently save the power budget for 6G green communication. In Fig. 3(b), it can be seen that exploiting the proposed ES protocols for STAR-RIS design shows superior outage performance compared to two benchmark protocols, mode-switching (labeled by "Mode.") and time-splitting (labeled by "Time."), when SWIPT-PS is exploited at N. This is because, in "Mode." protocols, the number of STAR-RIS elements used for reflective and reflection zones is reduced by half. Meanwhile, for "Time." protocols, the communication quality decreases significantly due to increased transmission delay, causing more error probability and thus increasing OP.

Fig. 4 shows the impact of the EH coefficient α (or β) and target rates r_f on the OPs of N, S, and F, where $K = 48$, $a = 0.8$, $b = 0.6$, and $r_f = r_s = 0.5$ bps/Hz. In Fig. 4(a), by letting $\rho = 7.5$ dB, $r_f = 0.5$, and $\Psi_N = \Psi_S = 0.01$, it is observed that when α (or β) increases, the time duration/power portion available for the EH process at N becomes larger, which increases the transmit power for the superposition coding of S and F. As a consequence, the OPs of S and F are improved. In particular, there exists an optimal point at

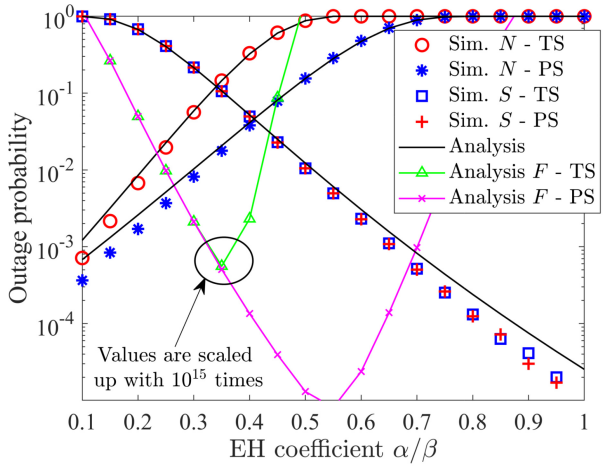

(a) Effects of α/β.

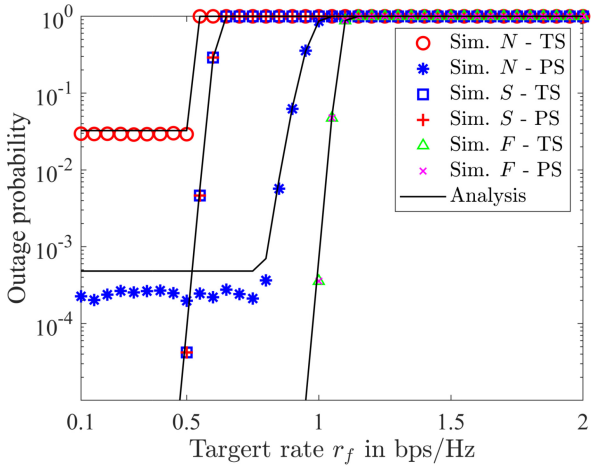

(b) Effects of r_f.

FIGURE 4. Effects of the EH coefficients and cell edges' target rate on the OP.

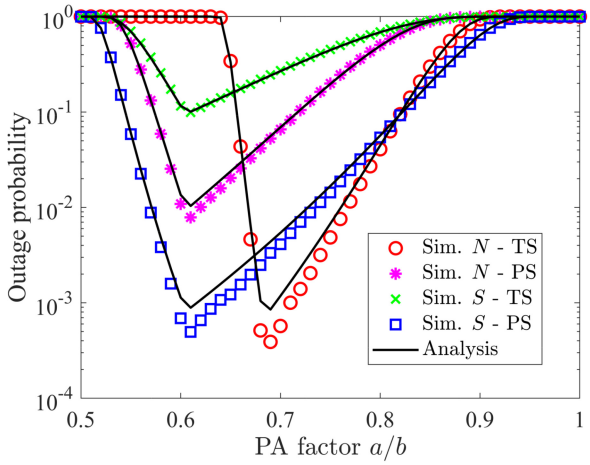

(a) OP at N and S

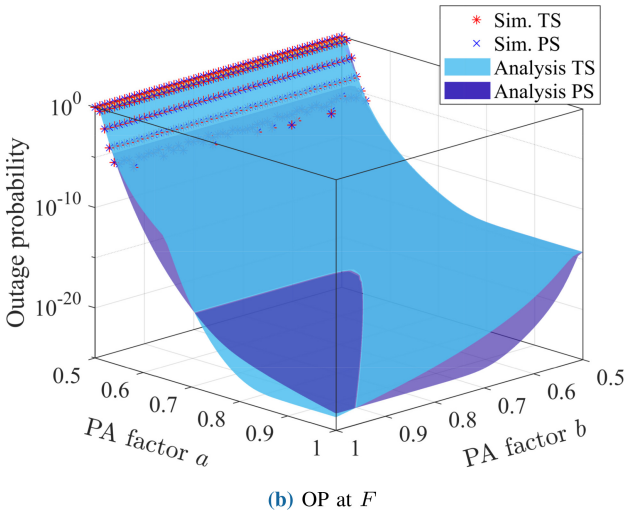

(b) OP at F

FIGURE 5. Effects of PA factors on the OP performance.

which the OP of F can be minimized. This is because the OP of F counts the outage event based on the decoding ability at N. On the one hand, when α (or β) is small, N is highly capable of decoding F's signal, but the harvested energy is quite small for serving cooperative communication. Thus, F can only rely on the SINR from direct communication, resulting in the constant OP. On the other hand, when α (or β) becomes larger, i.e., more energy harvests, F has a chance to improve its performance through cooperative communication, leading to OP improvement. However, it is worth noting that making α (or β) too large also increases the duration of the power portion used for information processing at N, which leads to an increase in its OP. In this case, F decodes its message from direct communication without any improvement. Moreover, exploiting PS protocols at N shows better performance than that of TS. This is because the use of PS protocols only reduces the quality of the received SINR, while for TS protocols, it directly causes a larger threshold decision ℓ for decoding x_f and x_n, leading to poor OP performance for N. In Fig. 4(b), by letting $\rho = 10$ dB, $\alpha = \beta = 0.5$ and $\Psi_N = \Psi_S = 0$, it is evident that when r_f becomes large, the chance of error in decoding increases, this increases the OPs of N and S. Meanwhile, the OP curves of F increase with r_f due to an increase in error data transmission probability.

Fig. 5 plots the OPs of N, S, and F as a function of PA factors a (or b) under settings of $\rho = 15$ dB, $\alpha = 0.3$, $\beta = 0.7$, $\Psi_N = \Psi_S = 0.01$, $K = 32$, $r_f = 0.5$ bps/Hz, and $r_s = r_n = 0.75$ bps/Hz. It is evident that smaller values of a (or b) result in an increased power budget allocated to N (or S)'s signal, decreasing the OP of N (or S), as depicted in Fig. 5(a). As a (or b) increases, the amount of power allocated to F increases, leading to a decrease in the OP of F, as depicted in Fig. 5(b). Both of these events reduce the OP of the system. Thus, there exists an optimal value a (or b) that minimizes system outage performance.

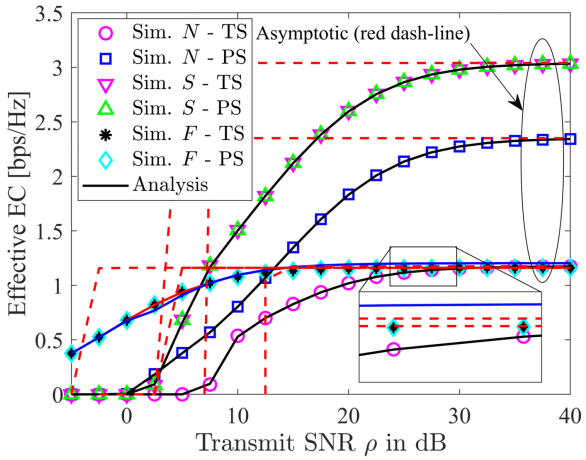

(a) Effect of ρ.

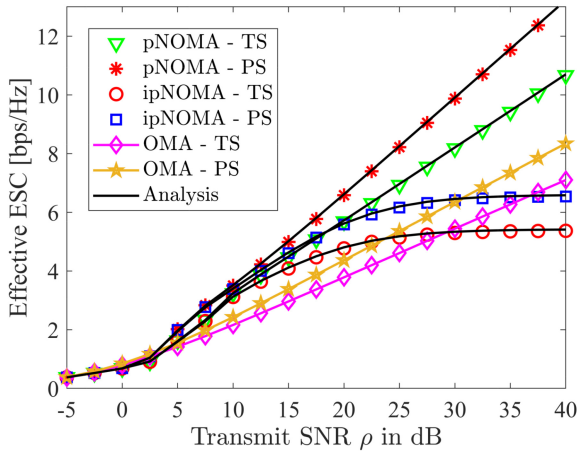

(b) ESC comparison.

FIGURE 6. Effective EC of nodes: a) Effect of ρ on and b) ESC comparison.

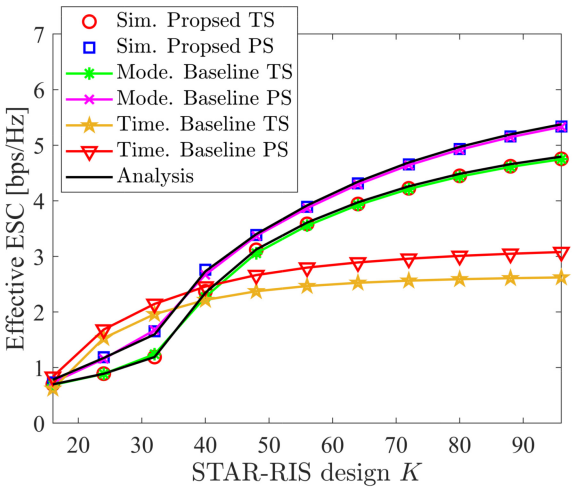

(a) STAR-RIS protocols.

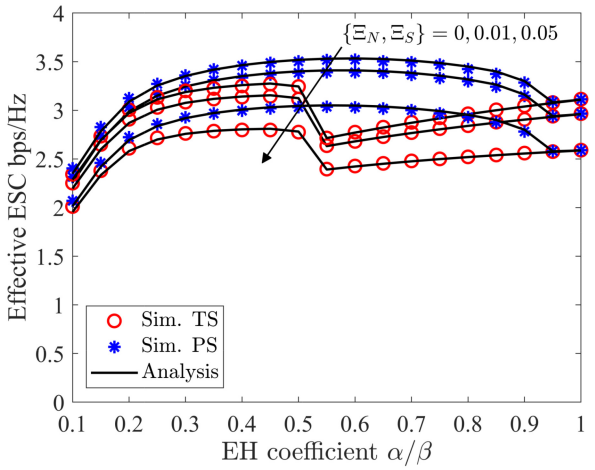

(b) Effects of α/β.

FIGURE 7. Effective ESC of nodes: a) ESC under different STAR-RIS protocols and b) Effects of α/β.

C. EFFECTIVE EC EVALUATION

By assuming that the threshold rates are $r_f = r_n = r_s = 0.5$ bps/Hz, Figs. 6-8 will first explore the impact of transmit SNR on the effective EC, then compare ergodic sum capacity (ESC) between NOMA and OMA, and finally observe the influence of PA factors and EH coefficients on ESC.

In Fig. 6, the effective EC is plotted as a function of transmit SNR ρ, where $a = 0.8$, $b = 0.6$, $\alpha = \beta = 0.5$, $\Psi_N = \Psi_S = 0.01$, and $K = 48$. It is observed from Fig. 6(a) that the effective ECs of N, S, and F increase with ρ in low as well as medium SNR regime and saturate in high SNR regime, which confirms the fact that the presence of imperfect SIC at N and S degrades their effective EC, whereas that of F is affected by the presence of unavoidable inter-user interference of N and S. In addition, the figure also shows that the EC performance of F and S does not change when using SWIPT-PS or SWIPT-TS criteria. Meanwhile, there is a significant EC distinction for N when adopting SWIPT-PS or SWIPT-TS. In particular, due to the shorter duration used for information processing in SWIPT-TS than in SWIPT-PS, this increases the outage performance for decoding x_f while also reducing the rate transmission capability by half. Next, Fig. 6(b) shows the ESC comparison between the proposed system with perfect SIC (pNOMA, $\Xi_N = \Xi_S = 0$) and imperfect SIC (ipNOMA, $\Xi_N = \Xi_S = 0.01$), and the baseline OMA system that exploits five orthogonal users' transmission time. As observed, when SIC operation is properly designed by N and F, the effective ESC linearly increases with the increment of transmit SNR and mostly outperforms its OMA counterparts. However, when the quality of SIC is poorly designed, the ESC of NOMA systems is degraded significantly and only outperforms OMA in the low-to-moderate SNR regime.

In Fig. 7, the impact of the number of STAR-RIS elements K as well as the way to split EH coefficients α (or β) on the effective EC performance is examined. By setting $\rho = 10$ dBm, $a = 0.8$, $b = 0.6$, $\alpha = \beta = 0.5$, and $\Psi_N = \Psi_S = 0.01$,

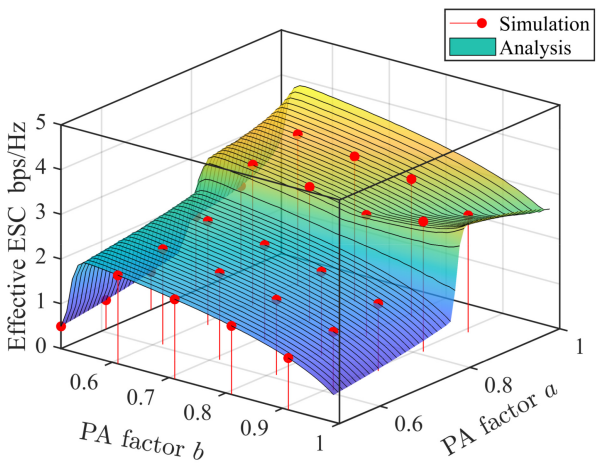

(a) SWIPT-TS exploitation.

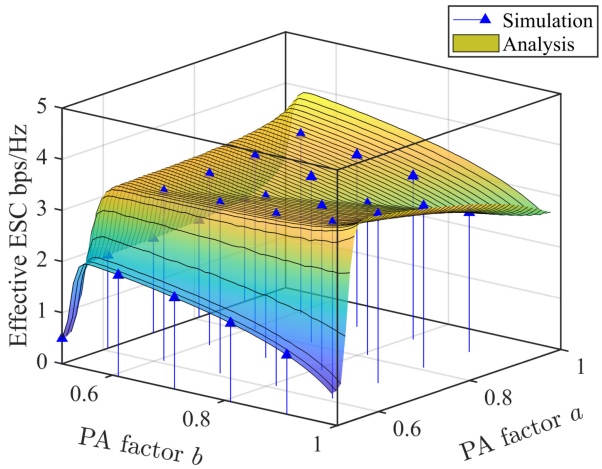

(b) SWIPT-PS exploitation.

FIGURE 8. Effective ESC of nodes vs *a* and *b*: a) SWIPT-TS and b) SWIPT-PS.

one can observe from Fig. 7(a) that the increasing number of STAR-RIS elements help in enhancing the systems' effective ESC. Besides, it also reveals that using the TS protocol turns back the best ESC improvement for less value of K. However, when K exceeds 40, it is clear that using the ES and "Mode." protocols yields a comparable ESC performance while outperforming "Time." ones. Taking into consideration the impact of imperfect SIC operation and $K = 48$, it can be seen from Fig. 7(b), that ESC is a concave function with β, while either concave/non-concave with respect to α. Obviously, when SWIPT-PS is used, the ESC can be maximized when β is set close to 0.6, while, for SWIPT-TS, the value of α should be around 0.45.

Finally, Fig. 8 quantifies the effect of PA factors on the effective ESC under settings of $\rho = 10$ dBm, $\alpha = \beta = 0.5$, $\Psi_N = \Psi_S = 0.01$, and $K = 48$. First, it can be observed from Fig. 8(a) that when SWIPT-TS is adopted, the ESC is a concave function with respect to b, and its maximum value varies around 0.55, whereas for a, the maximal ESC is obtained when a converges close to 1. Therefore, the reasonable PA solution for maximizing ESC should be $a \simeq 0.55$ and $b \simeq 0.9$. For SWIPT-TS adoptions, the result shows that the ESC reaches its maximum value when either $b \simeq 0.55$ and $a \simeq 0.9$ or $a \simeq 0.55$ and $b \simeq 0.9$.

V. CONCLUSION

This work proposed feasible solutions that exploit the interplay of caching and SWIPT adoptions in enhancing cell-edge users' performance of STAR-RIS-empowered NOMA systems. Taking two energy harvesting techniques into account, SWIPT-PS and SWIPT-PS, closed-form approximations and asymptotic expressions of the OP and effective EC were derived under practical imperfect SIC conditions. Numerical results not only corroborated the developed theoretical analyses but also confirmed the effectiveness of the proposed solution in improving cell-edge users' performance, the outstanding SWIPT-PS exploitation compared to the SWIPT-TS mechanism, the superiority of considered STAR-RIS-enabled ES protocols over mode-switching and time-splitting ones when deploying a large number of RIS elements, as well as the-out-of-box performance gain of NOMA over OMA signaling when dealing with properly SIC design.

Some interesting directions, which can be further extended from this work, include the consideration of multi-antenna system setup, transceiver and hardware impairments, inaccuracies/uncertainties channel estimation process, and co-channel interference, as well as the optimization of resource power allocation to minimize the outage performance and/or to maximize the ESC.

APPENDIX A
PROOF OF SECTION III-A

Following discrete phase-shift models, one has that X_s, Y_n, and Z_f can be rewritten, respectively, as

$$X_s = \sum_{k=1}^{K} \sqrt{\eta_k^s \Omega_{SR} \Omega_{RW}} |[\mathbf{g}_{SR}]_k| |[\mathbf{g}_{RW}]_k| e^{j\phi_e},$$

$$Y_n = \sum_{k=1}^{K} \sqrt{\eta_k^f \Omega_{SR} \Omega_{RF}} |[\mathbf{g}_{NR}]_k| |[\mathbf{g}_{RS}]_k| e^{j\phi_e},$$

$$Z_f = \sum_{k=1}^{K} \sqrt{\eta_k^f \Omega_{NR} \Omega_{RF}} |[\mathbf{g}_{NR}]_k| |[\mathbf{g}_{RF}]_k| e^{j(\phi_e + \arg(h_{NF}))} + \sqrt{\Omega_{NF}} |g_{NF}| e^{j \arg(h_{NF})}.$$

Since $|[\mathbf{h}_{RN}]_k|$ and $|[\mathbf{h}_{SR}]_k|$ are respectively equivalent to $|[\mathbf{h}_{NR}]_k|$ and $|[\mathbf{h}_{RS}]_k|$, thus it only sufficient to find the distributions of X_s and Z_f. Owing to $e^{j\phi} = \cos\phi + j\sin\phi$ and $|e^{j\phi}| = \cos^2\phi + \sin^2\phi = 1$, one can rewrite X_s and Z_f as

$$|X_s| = \sum_{k=1}^{K} A_W^s |[\mathbf{g}_{SR}]_k| |[\mathbf{g}_{RW}]_k| (\cos\phi_e + j\sin\phi_e),$$

$$|Z_f| = \sum_{k=1}^{K} B_F^f |[\mathbf{g}_{NR}]_k||[\mathbf{g}_{RF}]_k|(\cos\phi_e + j\sin\phi_e) + \sqrt{\Omega_{NF}}|g_{NF}|.$$

Recall that g_{TxRx} obeys Rayleigh distributions, and ϕ_e follows $\mathcal{U}(-2^{-q}\pi, 2^{-q}\pi)$, one has that

$$\mathrm{E}\{|g_{\mathrm{TxRx}}|\} = \sqrt{\pi}/2, \quad \mathrm{E}\{|g_{\mathrm{TxRx}}|^2\} = 1, \tag{A.1}$$

$$\mathrm{E}\{\cos\phi_e\} = \int_{\phi_e} \frac{\cos x}{2^{-q+1}\pi} dx = \frac{\sin\left(2^{-q}\pi\right)}{2^{-q}\pi}, \tag{A.2}$$

$$\mathrm{E}\{\cos^2\phi_e\} = \int_{\phi_e} \frac{\cos^2 x}{2^{-q+1}\pi} dx = \frac{1}{2} + \frac{\sin\left(2^{-q+1}\pi\right)}{2^{-q+2}\pi}, \tag{A.3}$$

$$\mathrm{E}\{\sin\phi_e\} = \int_{\phi_e} \frac{\sin x}{2^{-q+1}\pi} dx = 0, \tag{A.4}$$

$$\mathrm{E}\{\sin^2\phi_e\} = \int_{\phi_e} \frac{\sin^2 x}{2^{-q+1}\pi} dx = \frac{1}{2} - \frac{\sin\left(2^{-q+1}\pi\right)}{2^{-q+2}\pi}. \tag{A.5}$$

From (A.1) to (A.5) and the relation $\mathrm{Var}\{x\} = \mathrm{E}\{x^2\} - \mathrm{E}\{x\}^2$, one can arrive at the following distributions

$$\mathtt{Re}\{|X_s|\} \sim \mathcal{N}\left(\mu_{\mathrm{re}}^s, \sigma_{\mathrm{re}}^s\right), \mathtt{Im}\{|X_s|\} \sim \mathcal{N}\left(\mu_{\mathrm{im}}^s, \sigma_{\mathrm{im}}^s\right), \tag{A.6}$$

$$\mathtt{Re}\{|Z_f|\} \sim \mathcal{N}\left(\hat{\mu}_{\mathrm{re}}^f, \hat{\sigma}_{\mathrm{re}}^f\right), \mathtt{Im}\{|Z_f|\} \sim \mathcal{N}\left(\hat{\mu}_{\mathrm{im}}^f, \hat{\sigma}_{\mathrm{im}}^f\right), \tag{A.7}$$

where

$$\begin{aligned}
\mu_{\mathrm{re}}^s &= \mathrm{E}\{\mathtt{Re}\{|X_s|\}\} = KA_W^s \sin\left(2^{-q}\pi\right)/2^{-q+2},\\
\sigma_{\mathrm{re}}^s &= \mathrm{Var}\{\mathtt{Re}\{|X_s|\}\}\\
&= K\left(A_W^s\right)^2\left(\frac{1}{2} + \frac{\sin\left(2^{-q+1}\pi\right)}{2^{-q+2}\pi} - \frac{\sin^2\left(2^{-q}\pi\right)}{2^{-2q+4}}\right),\\
\mu_{\mathrm{im}}^s &= \mathrm{E}\{\mathtt{Im}\{|X_s|\}\} = 0,\\
\sigma_{\mathrm{im}}^s &= \mathrm{Var}\{\mathtt{Im}\{|X_s|\}\} = K\left(A_W^s\right)^2\left(\frac{1}{2} - \frac{\sin\left(2^{-q+1}\pi\right)}{2^{-q+2}\pi}\right),\\
\hat{\mu}_{\mathrm{re}}^f &= \mathrm{E}\{\mathtt{Re}\{|Z_f|\}\} = KB_F^f \frac{\sin\left(2^{-q}\pi\right)}{2^{-q+2}} + \sqrt{\Omega_{NF}}\frac{\sqrt{\pi}}{2},\\
\hat{\sigma}_{\mathrm{re}}^f &= \mathrm{Var}\{\mathtt{Re}\{|Z_f|\}\}\\
&= K\left(B_F^f\right)^2\left(\frac{1}{2} + \frac{\sin\left(2^{-q+1}\pi\right)}{2^{-q+2}\pi} - \frac{\sin^2\left(2^{-q}\pi\right)}{2^{-2q+4}}\right)\\
&\quad + \Omega_{NF}\left(1 - \frac{\pi}{4}\right),\\
\hat{\mu}_{\mathrm{im}}^f &= \mathrm{E}\{\mathtt{Im}\{|Z_f|\}\} = 0,\\
\hat{\sigma}_{\mathrm{im}}^f &= \mathrm{Var}\{\mathtt{Im}\{|Z_f|\}\} = K\left(B_F^f\right)^2\left(\frac{1}{2} - \frac{\sin\left(2^{-q+1}\pi\right)}{2^{-q+2}\pi}\right).
\end{aligned}$$

With (A.6) and (A.7) in hand, one can deduce that

$$\begin{aligned}
\mathrm{E}\{|X_s|^2\} &= \mathrm{E}\{(\mathtt{Re}\{|X_s|\} + \mathtt{Im}\{|X_s|\})^2\}\\
&= \mathrm{E}\{\mathtt{Re}\{|X_s|\}^2\} + 2\mathrm{E}\{\mathtt{Re}\{|X_s|\}\}\mathrm{E}\{\mathtt{Im}\{|X_s|\}\}\\
&\quad + \mathrm{E}\{\mathtt{Im}\{|X_s|\}^2\}\\
&= \sigma_{\mathrm{re}}^s + \left(\mu_{\mathrm{re}}^s\right)^2 + \sigma_{\mathrm{im}}^s,
\end{aligned} \tag{A.8}$$

$$\begin{aligned}
\mathrm{E}\{|X_s|^4\} &= \mathrm{E}\{(\mathtt{Re}\{|X_s|\} + \mathtt{Im}\{|X_s|\})^4\}\\
&= \mathrm{E}\{\mathtt{Re}\{|X_s|\}^4\} + \mathrm{E}\{\mathtt{Im}\{|X_s|\}^4\}\\
&\quad + 6\mathrm{E}\{\mathtt{Re}\{|X_s|\}^2\}\mathrm{E}\{\mathtt{Im}\{|X_s|\}^2\}\\
&\quad + 4\mathrm{E}\{\mathtt{Re}\{|X_s|\}\}\mathrm{E}\{\mathtt{Im}\{|X_s|\}^3\}\\
&\quad + 4\mathrm{E}\{\mathtt{Re}\{|X_s|\}^3\}\mathrm{E}\{\mathtt{Im}\{|X_s|\}\}\\
&= \left(\mu_{\mathrm{re}}^s\right)^4 + 6\left(\mu_{\mathrm{re}}^s\right)^2\sigma_{\mathrm{re}}^s + 3\left(\sigma_{\mathrm{re}}^s\right)^2\\
&\quad + 3\left(\sigma_{\mathrm{im}}^s\right)^2 + 6\left[\sigma_{\mathrm{re}}^s + \left(\mu_{\mathrm{re}}^s\right)^2\right]\sigma_{\mathrm{im}}^s,
\end{aligned} \tag{A.9}$$

$$\begin{aligned}
\mathrm{E}\{|Z_f|^2\} &= \mathrm{E}\{\left(\mathtt{Re}\{|Z_f|\} + \mathtt{Im}\{|Z_f|\}\right)^2\}\\
&= \mathrm{E}\{\mathtt{Re}\{|Z_f|\}^2\} + 2\mathrm{E}\{\mathtt{Re}\{|Z_f|\}\}\mathrm{E}\{\mathtt{Im}\{|Z_f|\}\}\\
&\quad + \mathrm{E}\{\mathtt{Im}\{|Z_f|\}^2\}\\
&= \hat{\sigma}_{\mathrm{re}}^f + \left(\hat{\mu}_{\mathrm{re}}^f\right)^2 + \hat{\sigma}_{\mathrm{im}}^s,
\end{aligned} \tag{A.10}$$

$$\begin{aligned}
\mathrm{E}\{|Z_f|^4\} &= \mathrm{E}\{\left(\mathtt{Re}\{|Z_f|\} + \mathtt{Im}\{|Z_f|\}\right)^4\}\\
&= \mathrm{E}\{\mathtt{Re}\{|Z_f|\}^4\} + \mathrm{E}\{\mathtt{Im}\{|Z_f|\}^4\}\\
&\quad + 6\mathrm{E}\{\mathtt{Re}\{|Z_f|\}^2\}\mathrm{E}\{\mathtt{Im}\{|Z_f|\}^2\}\\
&\quad + 4\mathrm{E}\{\mathtt{Re}\{|Z_f|\}\}\mathrm{E}\{\mathtt{Im}\{|Z_f|\}^3\}\\
&\quad + 4\mathrm{E}\{\mathtt{Re}\{|Z_f|\}^3\}\mathrm{E}\{\mathtt{Im}\{|Z_f|\}\}\\
&= \left(\hat{\mu}_{\mathrm{re}}^f\right)^4 + 6\left(\hat{\mu}_{\mathrm{re}}^f\right)^2\hat{\sigma}_{\mathrm{re}}^f + 3\left(\hat{\sigma}_{\mathrm{re}}^f\right)^2\\
&\quad + 3\left(\hat{\sigma}_{\mathrm{im}}^f\right)^2 + 6\left[\hat{\sigma}_{\mathrm{re}}^f + \left(\hat{\mu}_{\mathrm{re}}^f\right)^2\right]\hat{\sigma}_{\mathrm{im}}^s.
\end{aligned} \tag{A.11}$$

From (A.8) to (A.11), one can map the distributions of X_s and Z_f into Gamma distribution, by making the use of

$$\begin{aligned}
\kappa_s &= \frac{\mathrm{E}\{|X_s|^2\}^2}{\mathrm{Var}\{|X_s|\}} = \frac{\mathrm{E}\{|X_s|^2\}^2}{\mathrm{E}\{|X_s|^4\} - \mathrm{E}\{|X_s|^2\}^2}\\
&= \frac{\left(\sigma_{\mathrm{re}}^s + (\mu_{\mathrm{re}}^s)^2 + \sigma_{\mathrm{im}}^s\right)^2}{2\left[\left(\sigma_{\mathrm{re}}^s + (\mu_{\mathrm{re}}^s)^2 + \sigma_{\mathrm{im}}^s\right)^2 - \left(\mu_{\mathrm{re}}^s\right)^4\right]},
\end{aligned} \tag{A.12}$$

$$\begin{aligned}
\lambda_s &= \frac{\mathrm{Var}\{|X_s|\}}{\mathrm{E}\{|X_s|^2\}} = \frac{\mathrm{E}\{|X_s|^4\} - \mathrm{E}\{|X_s|^2\}^2}{\mathrm{E}\{|X_s|^2\}}\\
&= \frac{2\left[\left(\sigma_{\mathrm{re}}^s + (\mu_{\mathrm{re}}^s)^2 + \sigma_{\mathrm{im}}^s\right)^2 - \left(\mu_{\mathrm{re}}^s\right)^4\right]}{\sigma_{\mathrm{re}}^s + \left(\mu_{\mathrm{re}}^s\right)^2 + \sigma_{\mathrm{im}}^s},
\end{aligned} \tag{A.13}$$

$$\begin{aligned}
\tau_f &= \frac{\mathrm{E}\{|Z_f|^2\}^2}{\mathrm{Var}\{|Z_f|\}} = \frac{\mathrm{E}\{|Z_f|^2\}^2}{\mathrm{E}\{|Z_f|^4\} - \mathrm{E}\{|Z_f|^2\}^2}\\
&= \frac{\left(\hat{\sigma}_{\mathrm{re}}^s + (\hat{\mu}_{\mathrm{re}}^s)^2 + \hat{\sigma}_{\mathrm{im}}^s\right)^2}{2\left[\left(\hat{\sigma}_{\mathrm{re}}^s + (\hat{\mu}_{\mathrm{re}}^s)^2 + \hat{\sigma}_{\mathrm{im}}^s\right)^2 - \left(\hat{\mu}_{\mathrm{re}}^s\right)^4\right]},
\end{aligned} \tag{A.14}$$

$$\begin{aligned}
\theta_f &= \frac{\mathrm{Var}\{|Z_f|\}}{\mathrm{E}\{|Z_f|^2\}} = \frac{\mathrm{E}\{|Z_f|^4\} - \mathrm{E}\{|Z_f|^2\}^2}{\mathrm{E}\{|Z_f|^2\}}\\
&= \frac{2\left[\left(\hat{\sigma}_{\mathrm{re}}^s + (\hat{\mu}_{\mathrm{re}}^s)^2 + \hat{\sigma}_{\mathrm{im}}^s\right)^2 - \left(\hat{\mu}_{\mathrm{re}}^s\right)^4\right]}{\hat{\sigma}_{\mathrm{re}}^s + \left(\hat{\mu}_{\mathrm{re}}^s\right)^2 + \hat{\sigma}_{\mathrm{im}}^s}.
\end{aligned} \tag{A.15}$$

The proof is completed.

APPENDIX B
PROOF OF SECTION III-A
A. PROOF OF THEOREM 1

From (16), the OP of decoding x_n at N can be expressed as

$$P_{\mathrm{out}}^N = 1 - \Pr\left[\gamma_N^{x_f} \geq 2^{2r_f/\omega} - 1, \gamma_N^{x_n} \geq 2^{2r_n/\omega} - 1\right]$$

$$= 1 - \Pr\left[|X_n|^2 \geq \frac{\delta_f}{\varkappa\rho}, |X_n|^2 \geq \frac{\delta_n}{\varkappa\rho}\right]$$
$$= F_{|X_n|^2}\left(\frac{\max\{\delta_f, \delta_n\}}{\varkappa\rho}\right). \quad \text{(B.1)}$$

By plugging $F_{|X_n|^2}(\cdot)$ in (19) into (B.1), one can obtain the result in (35), and the proof ends.

B. PROOF OF THEOREM 2

After substituting (7) and (8) into (16), the OP at S can be rewritten as

$$P_{\text{out}}^S = 1 - \Pr\left[\gamma_S^{\bar{x}_f} \geq 2^{2r_f} - 1, \gamma_S^{x_s} \geq 2^{2r_s} - 1\right]$$
$$= \Pr\left[|X_n|^2|Y_n|^2 < \frac{\max\{\bar{\delta}_f, \bar{\delta}_n\}}{\nu\rho}\right]$$
$$= \int_0^\infty F_{|X_n|^2}\left(\frac{\max\{\bar{\delta}_f, \bar{\delta}_n\}}{\nu\rho y}\right) f_{|Y_n|^2}(y)dy. \quad \text{(B.2)}$$

By expressing $\Gamma(\kappa_n, \frac{x}{\lambda_n}) = G_{1,2}^{2,0}(\frac{x}{\lambda_n}|_{\kappa_n,0}^{1})$ and then invoking [52, eq. (9.31.2)], one has that $G_{1,2}^{2,0}(\frac{x}{\lambda_n}|_{\kappa_n,0}^{1}) = G_{2,1}^{0,2}(\frac{\lambda_n}{x}|_{0}^{1-\kappa_n,1})$. After plugging $F_{|X_n|^2}(\cdot)$ in (19) and $f_{|Y_n|^2}(\cdot)$ in (21) into (B.2), P_{out}^S can be rewritten as

$$P_{\text{out}}^S = 1 - \frac{1}{\Gamma(\kappa_n)} \int_0^\infty G_{2,1}^{0,2}\left(\frac{\nu\lambda_n\rho}{\max\{\bar{\delta}_f, \bar{\delta}_n\}} y \middle|_{0}^{1-\kappa_n, 1}\right)$$
$$\times \frac{y^{\kappa_n - 1}}{\Gamma(\kappa_n)(\lambda_n)^{\kappa_n}} \exp(-y/\lambda_n)dy. \quad \text{(B.3)}$$

Using [52, eqs. (7.813.1) and (9.31.2)], one can get the solution in (37), completing the proof.

C. PROOF OF THEOREM 3

From (18), the OP at F can be rewritten as

$$P_{\text{out}}^F = \Pr\left[\gamma_N^{x_f} \geq \ell_f, \gamma_F^{x_f} < \bar{\ell}_f, \gamma_F^{\bar{x}_f} < \bar{\ell}_f\right]$$
$$+ \Pr\left[\gamma_N^{x_f} < \ell_f, \gamma_F^{x_f} < \bar{\ell}_f\right]$$
$$= \begin{cases} J_1 + J_2, & \ell_f < \frac{a}{1-a} \wedge \bar{\ell}_f < \frac{a}{1-a} \wedge \bar{\ell}_f < \frac{b}{1-b}, \\ J_3, & \ell_f > \frac{a}{1-a} \wedge \bar{\ell}_f < \frac{a}{1-a} \vee \bar{\ell}_f < \frac{b}{1-b}, \\ 1, & \ell_f > \frac{a}{1-a} \wedge \bar{\ell}_f > \frac{a}{1-a} \wedge \bar{\ell}_f > \frac{b}{1-b}, \end{cases} \quad \text{(B.4)}$$

where

$$J_1 = \Pr\left[|X_n|^2 \geq \frac{\delta_f}{\varkappa\rho}, |X_f|^2 < \frac{\hat{\delta}_f}{\rho}, |X_n|^2|Z_f|^2 < \frac{\bar{\delta}_f}{\nu\rho}\right]$$
$$= F_{|X_f|^2}\left(\frac{\bar{\delta}_f}{\rho}\right) \int_0^\infty F_{|Z_f|^2}\left(\frac{\bar{\delta}_f}{\nu\rho x}\right) f_{|X_n|^2}(x)dx$$
$$- F_{|X_f|^2}\left(\frac{\bar{\delta}_f}{\rho}\right) F_{|X_n|^2}\left(\frac{\delta_f}{\varkappa\rho}\right)$$
$$- F_{|X_f|^2}\left(\frac{\bar{\delta}_f}{\rho}\right) \int_0^{\frac{\delta_f}{\varkappa\rho}} \left[1 - F_{|Z_f|^2}\left(\frac{\bar{\delta}_f}{\nu\rho x}\right)\right] f_{|X_n|^2}(x)dx, \quad \text{(B.5)}$$

$$J_2 = \Pr\left[\gamma_N^{x_f} < \ell_f, \gamma_F^{x_f} < \hat{\ell}_f\right]$$
$$= F_{|X_n|^2}\left(\frac{\delta_f}{\varkappa\rho}\right) F_{|X_f|^2}\left(\frac{\hat{\delta}_f}{\rho}\right), \quad \text{(B.6)}$$

$$J_3 = \Pr\left[\gamma_F^{x_f} < \hat{\ell}_f\right] = F_{|X_f|^2}\left(\frac{\hat{\delta}_f}{\rho}\right). \quad \text{(B.7)}$$

Making the same derivation as in (B.3), one can readily solve the first integral in (B.6) while the second integral can be approximated using Gauss-Chebyshev quadrature as in [51, eq. (45)]. With these outcome in hand, one first plugs $F_{|X_f|^2}(\cdot)$ into (B.6), (B.6), and (B.7), then substitutes $F_{|X_n|^2}(\cdot)$ into (B.6), and finally inserts the results of (B.6) and (B.6) into (B.4). After some algebraic steps, the final solution as in (39) is obtained, completing the proof.

REFERENCES

[1] F. Guo, F. R. Yu, H. Zhang, X. Li, H. Ji, and V. C. M. Leung, "Enabling massive IoT toward 6G: A comprehensive survey," *IEEE Internet Things J.*, vol. 8, no. 15, pp. 11891–11915, Aug. 2021.

[2] Palattella et al., "Internet of Things in the 5G era: Enablers, architecture, and business models," *IEEE J. Sel. Areas Commun.*, vol. 34, no. 3, pp. 510–527, Mar. 2016.

[3] C. Deng et al., "IEEE 802.11be wi-Fi 7: New challenges and opportunities," *IEEE Commun. Surveys Tuts.*, vol. 22, no. 4, pp. 2136–2166, 4th Quart., Jul. 2020.

[4] W. Ejaz, M. Naeem, A. Shahid, A. Anpalagan, and M. Jo, "Efficient energy management for the Internet of Things in smart cities," *IEEE Commun. Mag.*, vol. 55, no. 1, pp. 84–91, Jan. 2017.

[5] M. Giordani, M. Polese, M. Mezzavilla, S. Rangan, and M. Zorzi, "Toward 6G networks: Use cases and technologies," *IEEE Commun. Mag.*, vol. 58, no. 3, pp. 55–61, Mar. 2020.

[6] Y. Yuan et al., "NOMA for next-generation massive IoT: Performance potential and technology directions," *IEEE Commun. Mag.*, vol. 59, no. 7, pp. 115–121, Jul. 2021.

[7] L. Dai, B. Wang, Z. Ding, Z. Wang, S. Chen, and L. Hanzo, "A survey of non-orthogonal multiple access for 5G," *IEEE Commun. Surveys Tuts.*, vol. 20, no. 3, pp. 2294–2323, 3rd Quart., May 2018.

[8] F. Kara and H. Kaya, "Threshold-based selective cooperative-NOMA," *IEEE Commun. Lett.*, vol. 23, no. 7, pp. 1263–1266, Jul. 2019.

[9] X. Li, J. Li, Y. Liu, Z. Ding, and A. Nallanathan, "Residual transceiver hardware impairments on cooperative NOMA networks," *IEEE Trans. Wireless Commun.*, vol. 19, no. 1, pp. 680–695, Jan. 2020.

[10] O. Maraqa, A. S. Rajasekaran, S. Al-Ahmadi, H. Yanikomeroglu, and S. M. Sait, "A survey of rate-optimal power domain NOMA with enabling technologies of future wireless networks," *IEEE Commun. Survey Tuts.*, vol. 22, no. 4, pp. 2192–2235, 4th Quart., Aug. 2020.

[11] Y. Yuan et al., "5G non-orthogonal multiple access study in 3GPP," *IEEE Commun. Mag.*, vol. 58, no. 7, pp. 90–96, Jul. 2020.

[12] Y. Chen et al., "Toward the Standardization of non-orthogonal multiple access for next generation wireless networks," *IEEE Commun. Mag.*, vol. 56, no. 3, pp. 19–27, Mar. 2018.

[13] Q. Wu and R. Zhang, "Towards smart and reconfigurable environment: Intelligent reflecting surface aided wireless network," *IEEE Commun. Mag.*, vol. 58, no. 1, pp. 106–112, Jan. 2020.

[14] H. Yang et al., "Design of resistor-loaded reflectarray elements for both amplitude and phase control," *IEEE Antennas Wireless Propag. Lett.*, vol. 16, pp. 1159–1162, 2017.

[15] J.-C. Chen, "Beamforming optimization for intelligent reflecting surface-aided MISO communication systems," *IEEE Trans. Veh. Technol.*, vol. 70, no. 1, pp. 504–513, Jan. 2021.

[16] E. Björnson, Ö. Özdogan, and E. G. Larsson, "Intelligent reflecting surface versus decode-and-forward: How large surfaces are needed to beat relaying?," *IEEE Wireless Commun. Lett.*, vol. 9, no. 2, pp. 244–248, Feb. 2020.

[17] A. M. Salhab and M. H. Samuh, "Accurate performance analysis of reconfigurable intelligent surfaces over Rician fading channels," *IEEE Wireless Commun. Lett.*, vol. 10, no. 5, pp. 1051–1055, May 2021.

[18] D. Selimis, K. P. Peppas, G. C. Alexandropoulos, and F. I. Lazarakis, "On the performance analysis of RIS-empowered communications over Nakagami-m fading," *IEEE Commun. Lett.*, vol. 25, no. 7, pp. 2191–2195, Jul. 2021.

[19] M. A. Saeidi, M. J. Emadi, H. Masoumi, M. R. Mili, D. W. K. Ng, and I. Krikidis, "Weighted sum-rate Maximization for multi-IRS-assisted full-duplex systems with hardware impairments," *IEEE Trans. Cogn. Commun. Netw.*, vol. 7, no. 2, pp. 466–481, Jun. 2021.

[20] Y. Han, W. Tang, S. Jin, C.-K. Wen, and X. Ma, "Large intelligent surface-assisted wireless communication exploiting statistical CSI," *IEEE Trans. Veh. Technol.*, vol. 68, no. 8, pp. 8238–8242, Aug. 2019.

[21] S. Abeywickrama, R. Zhang, Q. Wu, and C. Yuen, "Intelligent reflecting surface: Practical phase shift model and beamforming optimization," *IEEE Trans. Commun.*, vol. 68, no. 9, pp. 5849–5863, Sep. 2020.

[22] Y. Wu, F. Zhou, W. Wu, Q. Wu, R. Q. Hu, and K. -K. Wong, "Multi-objective optimization for spectrum and energy efficiency tradeoff in IRS-assisted CRNs with NOMA," *IEEE Trans. Wireless Commun.*, vol. 21, no. 8, pp. 6627–6642, Aug. 2022.

[23] B. Lu, R. Wang, and Y. Liu, "Outage probability of intelligent reflecting surface assisted full duplex two-way communications," *IEEE Commun. Lett.*, vol. 26, no. 2, pp. 286–290, Feb. 2022.

[24] A. M. T. Khel and K. A. Hamdi, "Performance analysis of IRS-assisted full-duplex wireless communication systems with interference," *IEEE Commun. Lett.*, vol. 26, no. 9, pp. 2027–2031, Sep. 2022.

[25] Y. Ge and J. Fan, "Robust secure beamforming for intelligent reflecting surface assisted full-duplex MISO systems," *IEEE Trans. Inf. Forensics Security*, vol. 17, pp. 253–264, 2021.

[26] Z. Chu, W. Hao, P. Xiao, and J. Shi, "Intelligent reflecting surface aided multi-antenna secure transmission," *IEEE Wireless Commun. Lett.*, vol. 9, no. 1, pp. 108–112, Jan. 2020.

[27] S. Özyurt, A. F. Coşkun, S. Büyükçorak, G. K. Kurt, and O. Kucur, "A survey on multiuser SWIPT communications for 5G+," *IEEE Access*, vol. 10, pp. 109814–109849, 2022.

[28] X. Peng, P. Wu, H. Tan, and M. Xia, "Optimization for IRS-assisted MIMO-OFDM SWIPT system with nonlinear EH model," *IEEE Internet Things J.*, vol. 9, no. 24, pp. 25253–25268, Dec. 2022.

[29] C. Zhang, Y. Huang, C. He, C. Pan, and K. Wang, "Energy optimization for IRS-aided SWIPT under imperfect cascaded channels," *IEEE Trans. Veh. Technol.*, vol. 72, no. 9, pp. 11631–11643, Sep. 2023.

[30] M. Hua and Q. Wu, "Joint dynamic passive Beamforming and resource allocation for IRS-aided full-duplex WPCN," *IEEE Trans. Wireless Commun.*, vol. 21, no. 7, pp. 4829–4843, Jul. 2022.

[31] Y. Liu et al., "STAR: Simultaneous transmission and reflection for 360 coverage by intelligent surfaces," *IEEE Wireless Commun.*, vol. 28, no. 6, pp. 102–109, Dec. 2021.

[32] J. Xu, X. Mu, J. T. Zhou, and Y. Liu, "Simultaneously transmitting and reflecting (STAR)-RISs: Are they applicable to dual-sided incidence?," *IEEE Wireless Commun. Lett.*, vol. 12, no. 1, pp. 129–133, Jan. 2023.

[33] X. Mu, Y. Liu, L. Guo, J. Lin, and R. Schober, "Simultaneously transmitting and reflecting (STAR) RIS aided wireless communications," *IEEE Trans. Wireless Commun.*, vol. 21, no. 5, pp. 3083–3098, May 2022.

[34] J. Xu, Y. Liu, X. Mu, and O. A. Dobre, "STAR-RISs: Simultaneous transmitting and reflecting reconfigurable intelligent surfaces," *IEEE Commun. Lett.*, vol. 25, no. 9, pp. 3134–3138, Sep. 2021.

[35] M. Aldababsa, A. Khaleel, and E. Basar, "STAR-RIS-NOMA networks: An error performance perspective," *IEEE Commun. Lett.*, vol. 26, no. 8, pp. 1784–1788, Aug. 2022.

[36] T.-H. Vu, T.-V. Nguyen, Q.-V. Pham, D. B. da Costa, and S. Kim, "STAR-RIS-enabled short-packet NOMA systems," *IEEE Trans. Veh. Technol.*, vol. 72, no. 10, pp. 13764–13769, Oct. 2023.

[37] X. Li, Y. Zheng, M. Zeng, Y. Liu, and O. A. Dobre, "Enhancing secrecy performance for STAR-RIS NOMA networks," *IEEE Trans. Veh. Technol.*, vol. 72, no. 2, pp. 2684–2688, Feb. 2023.

[38] P. Zhao, J. Zuo, and C. Wen, "Power allocation and beamforming vectors optimization in STAR-RIS assisted SWIPT," in *Proc. IEEE Int. Conf. Commun. Technol.*, 2023, pp. 1174–1178.

[39] X. Qin, Z. Song, T. Hou, W. Yu, J. Wang, and X. Sun, "Joint resource allocation and configuration design for STAR-RIS-enhanced wireless-powered MEC," *IEEE Trans. Commun.*, vol. 71, no. 4, pp. 2381–2395, Apr. 2023.

[40] E. Bastug, M. Bennis, and M. Debbah, "Living on the edge: The role of proactive caching in 5G wireless networks," *IEEE Commun. Mag.*, vol. 52, no. 8, pp. 82–89, Aug. 2014.

[41] N. Zhao, X. Liu, F. R. Yu, M. Li, and V. C. M. Leung, "Communications, caching, and computing oriented small cell networks with interference alignment," *IEEE Commun. Mag.*, vol. 54, no. 9, pp. 29–35, Sep. 2016.

[42] R. Wang, J. Zhang, S. H. Song, and K. B. Letaief, "Mobility-aware caching in D2D networks," *IEEE Trans. Wireless Commun.*, vol. 16, no. 8, pp. 5001–5015, Aug. 2017.

[43] M. Yang, J. Chen, L. Yang, L. Lv, B. He, and B. Liu, "Design and performance analysis of cooperative NOMA with coordinated direct and relay transmission," *IEEE Access*, vol. 7, pp. 73306–73323, 2019.

[44] A. Jee, K. Agrawal, and S. Prakriya, "A coordinated direct AF/DF relay-aided NOMA framework for low outage," *IEEE Trans. Commun.*, vol. 70, no. 3, pp. 1559–1579, Mar. 2022.

[45] A. Jee and S. Prakriya, "Performance of energy and spectrally efficient AF relay-aided incremental CDRT NOMA based IoT network with imperfect SIC for smart cities," *IEEE Internet Things J.*, vol. 10, no. 21, pp. 18766–18781, Nov. 2022,

[46] H. B. Mahmoodi, J. Kaleva, S. P. Shariatpanahi, and A. Tölli, "D2D assisted multi-antenna coded caching," *IEEE Access*, vol. 11, pp. 16271–16287, 2023.

[47] Y. Cai and A. F. Molisch, "On the multi-activation oriented design of D2D-aided caching networks," in *Proc. IEEE Global Commun. Conf.*, 2019, pp. 1–6.

[48] X. Zhang, T. Lv, Y. Ren, and Z. Lin, "Joint content push and transmission in NOMA with SWIPT caching helper," *IEEE Commun. Lett.*, vol. 24, no. 4, pp. 922–925, Apr. 2020.

[49] Y. Ren, K. Qian, X. Zhang, F. Jiang, and G. Lu, "Joint power and time allocation in NOMA-SWIPT enabled wireless caching networks," in *Proc. IEEE Veh. Technol. Conf.*, 2023, pp. 1–5.

[50] A. K. Shukla, J. M. Moualeu, M. Magarini, and P. K. Upadhyay, "Performance analysis of cache- and SWIPT-aided NOMA-based CDRT networks," in *Proc. IEEE Int. Telecommun. Conf.*, 2023, pp. 254–259.

[51] T.-H. Vu, T.-V. Nguyen, and S. Kim, "Cooperative NOMA-enabled SWIPT IoT networks with imperfect SIC: Performance analysis and deep learning evaluation," *IEEE Internet Things J.*, vol. 9, no. 3, pp. 2253–2266, Feb. 2022.

[52] A. Jeffrey and D. Zwillinger, *Table of Integrals, Series, and Products*. Amsterdam, The Netherlands: Elsevier, 2007.

[53] Dhirendra, "Bivariate Meijer G-function: Implementation in MATLAB," Linkedin.com. Accessed: Sep. 20, 2020. [Online]. Available: https://www.linkedin.com/embed/feed/update/urn:li:ugcPost:6713378315895369728

[54] M. Vaezi, R. Schober, Z. Ding, and H. V. Poor, "Non-orthogonal multiple access: Common myths and critical questions," *IEEE Wireless Commun.*, vol. 26, no. 5, pp. 174–180, Oct. 2019.

[55] A. A. Nasir, X. Zhou, S. Durrani, and R. A. Kennedy, "Relaying protocols for wireless energy harvesting and information processing," *IEEE Trans. Wireless Commun.*, vol. 12, no. 7, pp. 3622–3636, Jul. 2013.

[56] M. K. Simon and M.-S. Alouini, *Digital Communication Over Fading Channels*. Hoboken, NJ, USA: Wiley, 2005. [Online]. Available: https://ieeexplore.ieee.org/book/5238261

[57] T.-H. Vu and S. Kim, "Performance evaluation of power-beacon-assisted wireless-powered NOMA IoT-based systems," *IEEE Internet Things J.*, vol. 8, no. 14, pp. 11655–11665, Jul. 2021.

[58] "Meijer G-function: Integration," Wolfram.com. Oct. 2001. [Online]. Available: https://functions.wolfram.com/HypergeometricFunctions/MeijerG/21/02/04/0001/